2018-12-01

Property Localization for Grain Boundary Diffusivity via Inverse Problem Theory

Christian Kurniawan
Brigham Young University

Property Localization for Grain Boundary Diffusivity via Inverse Problem Theory

Christian Kurniawan

A thesis submitted to the faculty of
Brigham Young University
in partial fulfillment of the requirements for the degree of

Master of Science

Oliver K. Johnson, Chair
David T. Fullwood
Eric R. Homer

Department of Mechanical Engineering

Brigham Young University

ABSTRACT

Property Localization for Grain Boundary Diffusivity
via Inverse Problem Theory

Christian Kurniawan
Department of Mechanical Engineering, BYU
Master of Science

The structure and spatial arrangement of grain boundaries strongly affect the properties of polycrystalline materials such as corrosion, creep, weldability, superconductivity, and diffusivity. However, constructing predictive grain boundary structure-property models is taxing, both experimentally and computationally due to the high dimensionality of the grain boundary character space. The purpose of this work is to develop an effective method to infer grain boundary structure-property models from measurement of the effective properties of polycrystals by utilizing the inverse problem theory. This study presents an idealized case in which structure-property models for grain boundary diffusivity are inferred from a noisy simulation.

The method presented in this study is derived from a general mathematical expression of inverse problem theory. The derivation of the method is carried step by step by considering diffusivity as the property of interest. The use of the Bayesian probability approach in the inference method makes the uncertainty quantification possible to perform. This study demonstrates how uncertainty quantification for the inferred structure-property models is easily performed within the idealized case framework. The method of quantifying the uncertainty is carried by utilizing the Metropolis-Hastings algorithm and Kernel Density Estimation method.

The validation of the method is carried out by considering structure-property models with one, three, and five degrees of freedom. Two- and three-dimensional simulated polycrystals are used in this study to obtain the simulation data. The two-dimensional simulated polycrystals used in this study are generated using grain growth simulation performed using a front-tracking algorithm. The three-dimensional polycrystals used in this study are generated using Neper software resulting in a real-like polycrystals. The structure-property models used in the validation are picked by considering the qualitative features that reflect trends observed in literature. The inference method is performed by ignoring any knowledge about the structure-property model in the process.

Keywords: Grain Boundary, Structure-Property Model, property localization, Grain Boundary Diffusivity, inference, Inverse Problem Theory

ACKNOWLEDGMENTS

I would first like to thank my graduate committee chair, Dr. Oliver K. Johnson of the Mechanical Engineering Department at Brigham Young University. Dr. Johnson was always there to help whenever I ran into trouble spots or had questions about research or writing. He steered me in the right direction but also allowed me to grow. His guidance helped me to improve and to become a better researcher. I would also like to thank my other graduate committee members, Dr. Eric R. Homer, and Dr. David T. Fullwood, who were always there to help and support me with their expertise during the process of researching and writing this thesis.

I would thank Jarrod M. Lund and Tyler R. Critchfield for their assistance in providing the 1771 two dimensional polycrystal templates. I would also like to show my gratitude for the guidance and insights from David Page, Akash Amalaraj, and my other colleagues in the material science lab at Brigham Young University during the course of this research.

Finally, I must express my very profound gratitude to my family for providing me with unfailing support and continuous encouragement throughout my years of study, research, and writing this thesis. This accomplishment would not have been possible without them.

The material presented here is based upon work supported by the National Science Foundation under Grant No. 1610077. Any opinions, findings, and conclusions or recommendations expressed in this material are those of me as the author and do not necessarily reflect the views of the National Science Foundation. Most of the content in this thesis is taken from the publication manuscript number A-18-2959 submitted to Acta Materilia in August 2018.

TABLE OF CONTENTS

LIST OF TABLES . . . . . **v**

LIST OF FIGURES . . . . . **vi**

NOMENCLATURE . . . . . **viii**

Chapter 1 Introduction **1**

Chapter 2 Background **4**
2.1 Grain Boundaries 4
2.1.1 Grain Boundary Structure 5
2.1.2 Grain Boundary Structure-Property Model 5
2.2 Homogenization 7
2.3 Property Localization 9

Chapter 3 Method **11**
3.1 Inverse Problem Theory 11
3.2 GB Property Localization 13
3.3 Uncertainty Quantification 17

Chapter 4 Validation **19**
4.1 Microstructures Generation 19
4.2 Obtaining Effective Diffusivity 21
4.3 Inferring and Validating 22

Chapter 5 Results and Discussion **24**
5.1 Validation Results 24
5.1.1 1 DOF Validation Results 24
5.1.2 3 DOF Validation Result 26
5.1.3 5 DOF Validation Result 28
5.2 Discussion 31
5.2.1 Inference Accuracy 31
5.2.2 Influence of GBCD 32
5.2.3 Influence of Discretization Resolution and Number of Microstructures . . . 33
5.2.4 Limitations of the Piece-wise Constant Function 35
5.2.5 Singularity 38

Chapter 6 Conclusion **40**

REFERENCES **43**

LIST OF TABLES

5.1 Average integrated relative error of the inferred models. 32

LIST OF FIGURES

2.1 Illustration of GB where it can be thought of as two dimensional planes that separate grains in materials (left adapted from [1]; right adapted from [2]). 4
2.2 Illustration of GB where disorientation of grain A and grain B is represented by (ω, θ, ϕ) and the normal of the boundary plane is represented by (α, β); adapted from [3,4]. . . 5
2.3 Comparison of the Read-Shockley model and the actual value energy of silicon ferrite. The dashed line is the function of Equation (2.1) and the dots are the actual data. The picture is directly taken from [5]. 6
2.4 Computed GB energy of Ni plotted against the disorientation angle between two grain (left) and Σ (right). The picture is taken from [6]. 7

3.1 Illustration of the uncertainty quantification method. (a) Contour plot of $\sigma(\{\mathbf{D}, \mathbf{M}\})$ with the marginal densities for each dimension shown as dotted lines. (b) The corresponding structure-property model ($\mathscr{D}$), discretized into two bins. 17

4.1 Example of a two-dimensional polycrystal template used in this study. Colors indicate crystallographic orientation, as shown in the accompanying inverse pole figure (IPF) color legend. 19
4.2 Example of a three-dimensional polycrystal template used in this study with crystallographic orientation is represented using IPF coloring. 20

5.1 Comparison between the inferred model and the true model for (a) the 1DOF BRK function and (b) the exponential function of Equation (5.2), together with quantified inference uncertainty. The disorientation angle distribution across all of the employed microstructures is shown in histogram form above each plot. 26
5.2 (a) Comparison between the true (left) and the inferred (right) 3DOF GB diffusivity structure-property model, displayed in the Rodriguez space parameterization of the disorientation FZ. (b) The magnitude of the 95% confidence interval for the inference in each bin (a measure of the uncertainty in the inference). Interior lines define the boundaries of the tetrahedral bins. To facilitate visualization of the uncertainty in the interior of the FZ, the tetrahedral bins are slightly reduced in size in (b). 27
5.3 Comparison between the true and the inferred 5DOF GB diffusivity structure-property model. Each big circle is the stereographic projection of the hemisphere (GB plane FZ) corresponding to the center of the bin in the disorientation FZ, displayed in the Rodriguez space, which is specified by the numbering of the point. The color of the hemisphere represents the true diffusivity value and the small circular markers indicate the inferred diffusivity value in each bin using the same color scale. 29
5.4 Plots of the 95% confidence interval's magnitude for the inference in each bin (a measure of the uncertainty in the inference) shown as the color of the hemisphere with accompanying colormap. 30
5.5 The GBCD for the 5DOF case across all of the employed polycrystals to obtain inference result displayed in Figure 5.3. 32

5.6 Comparison of the average integrated relative error of the inference using different numbers of bins and microstructures. In this comparison, we used the 1DOF BRK model. The color-scale is clipped at 5% so that the region of interest, which has low error, is visible; however, higher errors were observed when the number of bins was extremely small. 33
5.7 Illustration of the KDE approach. The figure shows the 1DOF case where the domain is discretized into five bins. The colored lines are the approximate constitutive models obtained from the inference processes with different set of polycrystals (each model is indicated by the same line's color). The dashed black line at each bin is the estimated density distribution. The black lines are the model from the optimum density. The dashed gray line is the actual model. 35
5.8 GB property localization result utilizing the KDE approach, applied to the problem presented in Section 5.1.3. Each big circle is the stereographic projection of the hemisphere (GB plane FZ) corresponding to the center of the bin in the disorientation FZ. The color of the hemisphere represents the true diffusivity value and the small circular markers indicate the inferred diffusivity value in each bin using the same color scale. . 36
5.9 GB property localization result utilized the KDE approach, applied to the problem where $\varepsilon \sim N\left[0, \left(0.5\% \left(\bar{D}^{\mathrm{SGT}}\right)\right)^2\right]$ noise to Equation (4.1) is introduced. Each big circle is the stereographic projection of the hemisphere (GB plane FZ) corresponding to the center of the bin in the disorientation FZ. The color of the hemisphere represents the true diffusivity value and the small circular markers indicate the inferred diffusivity value in each bin using the same color scale. 37
5.10 The average integrated relative error in each bin for (a) the 1DOF BRK model case and (b) 1DOF exponential function of Equation (5.2). In contrast to Figure 5.1, both models are plotted on a linear scale to clearly highlight which regions have small vs. large gradients with the blue lines indicate the approximate gradient of the functions. . 38

NOMENCLATURE

1DOF	The case where the GB structure-property model has only have one degree of freedom (the disorientation angle with the same axis rotation for each grain)
3DOF	The case where the GB structure-property model has three degrees of freedom (the angle and axis of the disorientation)
5DOF	The case where the GB structure-property model has five degrees of freedom (the angle and axis of the disorientation as well as the normal of the GB plane)
A	cross sectional area
(d)	measurements/observations of a system
D	diffusivity
$\bar{D}$	effective diffusivity
$\bar{D}^{obs}$	observed effective diffusivity
$\bar{D}^{SGT}$	the effective diffusivity predicted using the SGT-method
$\mathscr{D}$	a function that abstractly represents the GB diffusivity structure-property model
$\widehat{\mathscr{D}}$	piecewise-constant approximation to $\mathscr{D}$
E	energy
E_{GB}	GB energy
EBSD	Electron Back-Scatter Diffraction
EMT	Effective Medium Theory
GB	Grain Boundary
GBCD	Grain Boundary Character Distribution
GBE	Grain Boundary Engineering
GBN	Grain Boundary Network
GEM	General Effective Medium
H	homogenization relation
k	normalization constant
KDE	Kernel Density Estimation
L	length
$\mathscr{L}$	the diffusivity-weighted GBN Laplacian matrix
(m)	model parameters that characterize a system
M	microstrcutural information
PDF	Probability Density Function
s	standard deviation
SGT	Spectral Graph Theory
$u_k(a)$	a-th element of the k-th eigenvector
UQ	Uncertainty Quantification
(α, β)	parameters to represent the normal vector of GB plane
$\delta()$	delta-dirac function
Θ	probability density function of the theoretical state of information
(θ, ϕ)	parameters to represent a rotation axis of two adjacent grains
λ	eigenvalue of a matrix

μ	the homogenous state of information
ρ	probability density function of the *a priori* state of information
σ	probability density function of the *a posteriori* state of information
ω	misorientation or disorientation angle of two adjacent grains

CHAPTER 1. INTRODUCTION

A grain boundary (GB) is the interfacial transition between two adjacent grains in a polycrystalline material. GBs play many important roles in material phenomena and in many cases govern numerous properties of crystalline materials. For example, the structure and spatial arrangement of GBs strongly affect the corrosion [7], creep [8], weldability [9], superconductivity [10], and diffusivity [11, 12] of polycrystalline materials. Grain boundary engineering (GBE) demonstrates that material properties can be enhanced by controlling the population of different GB types [7, 13–18]. Therefore, if we can have the GB structure-property model, we can apply GBE techniques to accelerate the discovery of new materials with more desirable properties.

Efforts to develop GB structure-property models have historically relied on experiments or atomistic calculations performed on bicrystals [6, 19–21]. However, due to the high dimensionality of the GB configuration space, measuring and/or calculating GB properties one-by-one has limited the scope of investigations primarily to a relatively small set of highly symmetric GB types [22]. This has greatly hampered the development of GB structure-property models, and at present, such models are few in number and are limited to incomplete portions of the five-dimensional GB character space (e.g. the Read-Shockley model [5]). Only recently has the first GB structure-property model over the five-dimensional GB character space been developed [23], allowing for prediction of GB energy in FCC metals.

In contrast to bicrystals, polycrystals are easier and less expensive to manufacture and each polycrystalline sample contains a large number of GBs. Thus, a more efficient strategy for inferring GB structure-property models might be to rely on measurements of the effective properties of polycrystals. The challenge for such an approach lies in the deconvolution of the respective contributions of each GB. In essence, I propose that exchanging a small quantity of data that is highly precise (bicrystals) for a large quantity of data that has greater uncertainty (polycrystals) may be the key to making the problem tractable.

Because it is the inverse of the problem of *homogenization*, this problem of inferring constituent properties from the effective properties of a material is referred to as *property localization*[1]. Although relatively unstudied, there are a few examples of localization problems in the literature in which single crystal elastic constants were obtained from measurements of the elastic response of polycrystals [31–33].

Johnson, Li, Demkowicz, and Schuh [34] have recently applied the property localization concept to GBs to infer the parameters of a structure-property model for GB diffusivity from synthetic idealized two-dimensional polycrystals with honeycomb geometry. In their work, the inverse problem of GB property localization was solved by regression with an analytical *ansatz* (i.e. the form of the structure-property model was known *a priori*). Although successful, the requirement of an analytical *ansatz* is a significant limitation because for many GB properties, including diffusivity, the functional form of the structure-property model is unknown; in fact, the model form is precisely the information one hopes to learn by the inference effort.

In this work, I develop a new approach for GB property localization based on Bayesian strategies employed in inverse problem theory. In addition to eliminating the requirement for an analytical *ansatz*, the new method naturally facilitates uncertainty quantification for the inferred structure-property model. To validate the new approach, I infer structure-property models for GB diffusivity from calculations of the effective diffusivity of realistic two- and three-dimensional polycrystals, without using *a priori* information about the form of the constitutive models. By enabling the use of simple to manufacture, data-rich polycrystals (instead of reliance on bicrystals), it is anticipated that this new strategy will make tractable the problem of inferring structure-property models for GBs.

In this thesis, I will describe how an inverse problem theory can be used to infer GB structure-property models. Here, the related information and the derivation of the method will be presented. The derivation of the method will focus on the diffusivity property. However, the general form of the method can be used in other applications to infer the constitutive models of numerous GB properties. The validation of the method will be carried out by considering the case where the GB structure-property models have one, three, and five degrees of freedom. Two- and

[1]Term "property localization" is used to distinguish this problem from the more frequently studied problem of inferring the local state (e.g. the local stress tensor) from the macroscopic state (e.g. the effective stress tensor) of a polycrystal [24–30], which I refer to as "state localization".

three-dimensional simulated polycrystals are used in this thesis to obtain the effective diffusivity calculations as well as the other observable information needed. The method of quantifying the uncertainty will also be presented here.

To describe the relevant theory and demonstrate its application for an idealized model system, in an effort to validate the approach, the thesis is organized as follows. Chapter 2 explains the relevant and necessary theories in the study. Chapter 3 describes the derivation of the GB property localization method and its uncertainty quantification. Chapter 4 explains the method to validate the inference process. Chapter 5 presents the result of the validation.

CHAPTER 2. BACKGROUND

Relevant information about the GBs and the property localization method will be introduced in this chapter.

2.1 Grain Boundaries

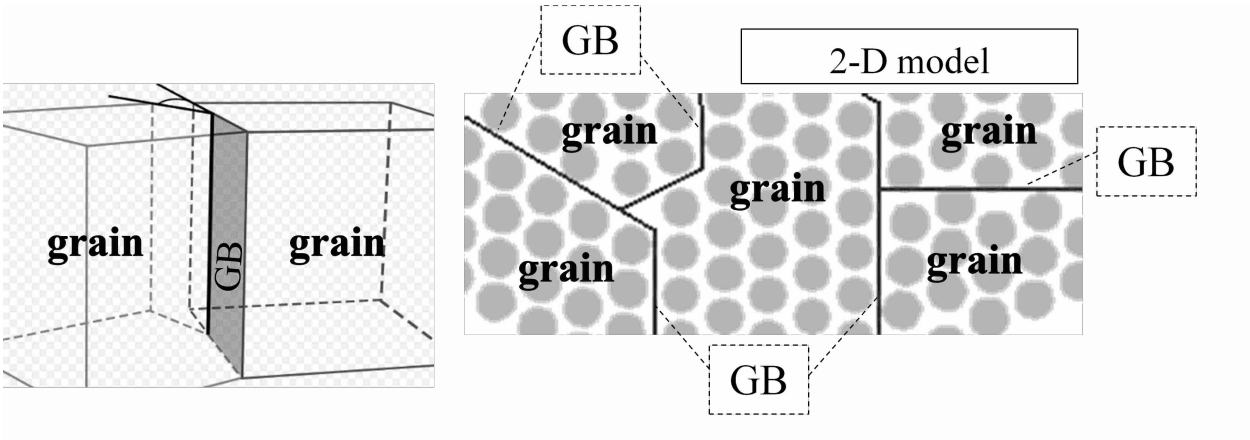

Figure 2.1: Illustration of GB where it can be thought of as two dimensional planes that separate grains in materials (left adapted from [1]; right adapted from [2]).

GBs are the interfacial transition between two touching grains/crystals which have different crystallographic orientation [19, 35] (see Figure 2.1). Because a GB is separating two adjacent grains, it can also be thought of as the interfacial defect which affects numerous properties of the material. In the two-dimensional illustration of Figure 2.1, GBs can be noticed from the atomic mismatch when the transition in crystalline orientation of two adjacent grains occurs. This mismatch can be quantified using the misorientation of the adjacent grains and the direction of the GB plane which can be used to characterize the GB type and will be explained further in Section 2.1.1 below.

2.1.1 Grain Boundary Structure

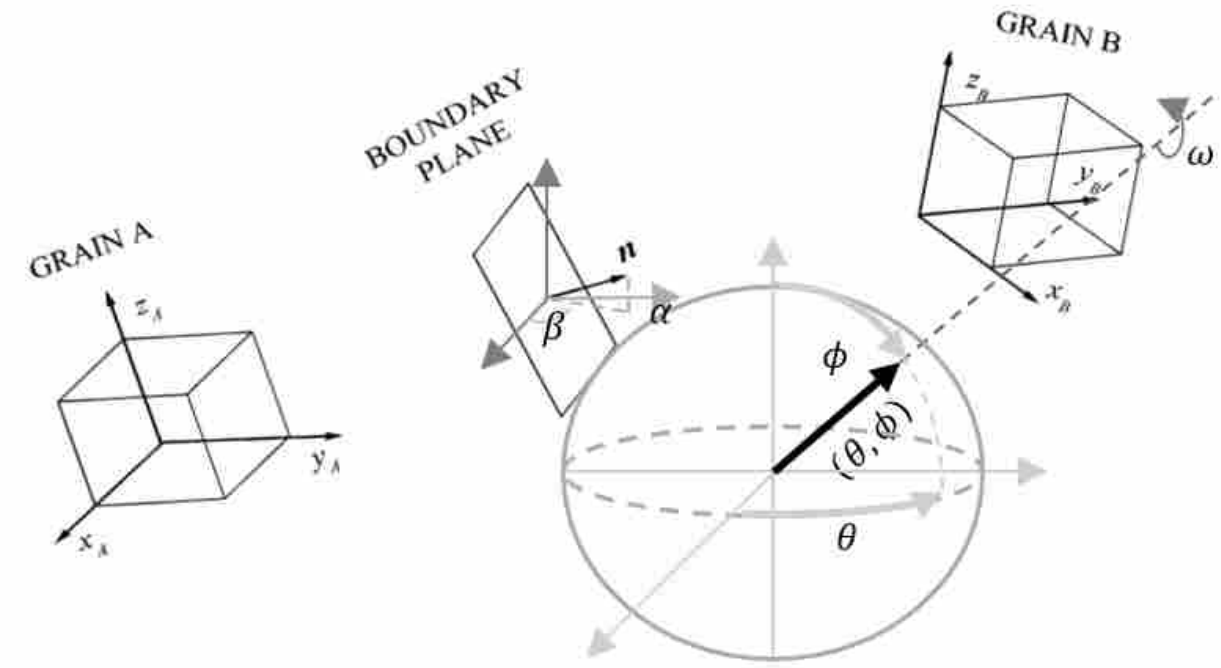

Figure 2.2: Illustration of GB where disorientation of grain A and grain B is represented by (ω, θ, ϕ) and the normal of the boundary plane is represented by (α, β); adapted from [3, 4].

The structure of a GB can be characterized by its five degrees of freedom to describe [36]. There are two common methods describing these five degrees of freedom to characterize GB crystallography as explained by Olmsted [37]. This study will use two parameters to describe the normal of the boundary plane (α, β); while the grain disorientation will be described using two parameters to represent the rotation axis (θ, ϕ) and another parameter to represent the rotation to bring the grains in perfect matching ω [3, 4, 23] (see Figure 2.2).

2.1.2 Grain Boundary Structure-Property Model

The function that relates the GB structure to its properties is commonly referred to as GB structure-property model. One of the earliest studies of GB structure-property models was conducted by Read and Shockley [5] which approximate GB energy by treating it as an array of dislocations. The model presented in [5], commonly known as the Read-Shockley model, is

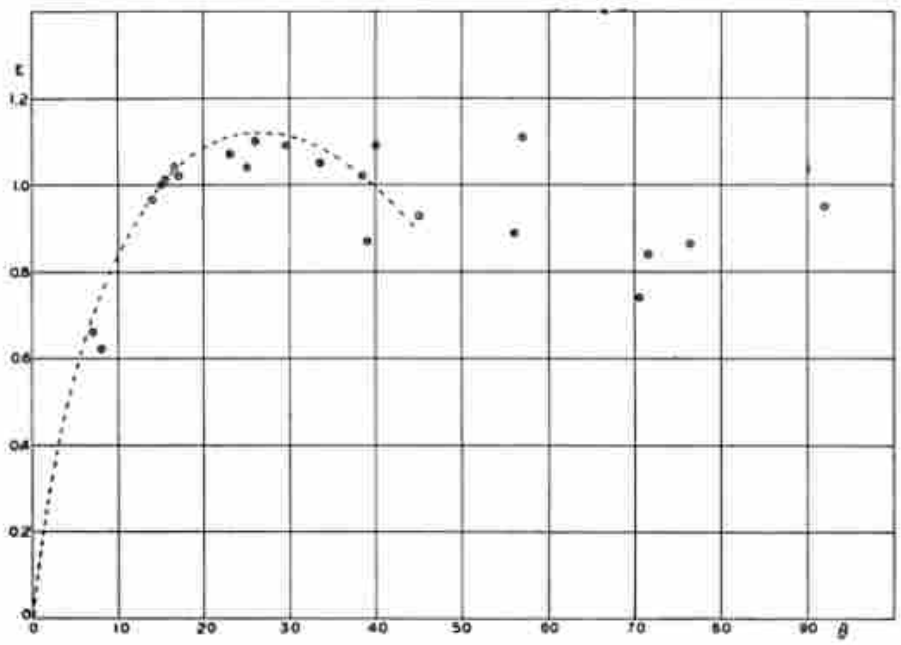

Figure 2.3: Comparison of the Read-Shockley model and the actual value energy of silicon ferrite. The dashed line is the function of Equation (2.1) and the dots are the actual data. The picture is directly taken from [5].

the function of dislocation energy and GB disorientation angle ($E_{GB} = f(\omega, E_{\perp})$). The model is commonly written as:

$$E = E_0 \omega (A - \ln \omega) \tag{2.1}$$

where ω is the disorientation angle of the neighboring grains and A is a parameter that depends on the GB plane which commonly is assumed to be constant. The model is commonly used with only one degree of freedom (ω) in the calculation and is only accurate for small values of ω (see Figure 2.3).

A study conducted by Olmsted [6] observed that GBs with the same disorientation angle can have substantially different energies as shown in Figure 2.4. This result led to the conclusion that disorientation angle alone is insufficient to determine the GB energy. By interpolating the data presented by [6], Bulatov, Reed, and Kumar successfully represent the energy of GB in a function of its complete five degrees of freedom [23], referred to as the BRK-energy model in this study.

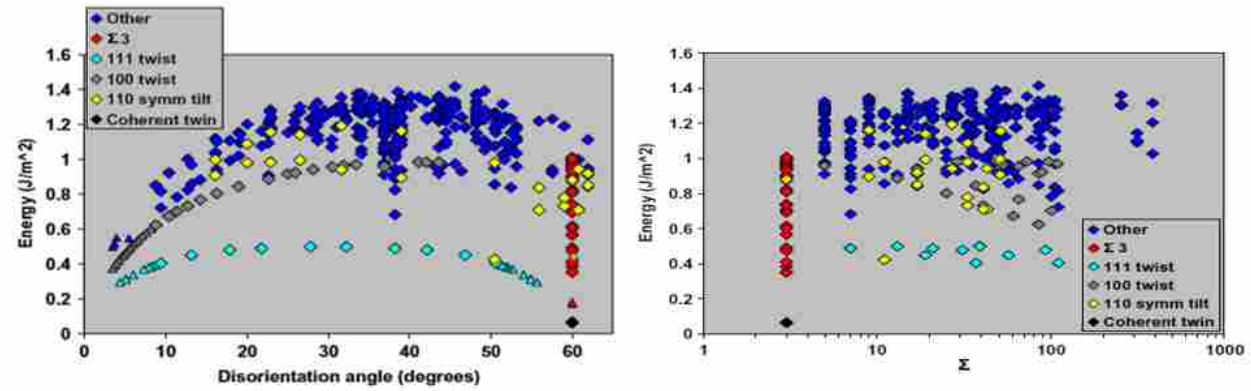

Figure 2.4: Computed GB energy of *Ni* plotted against the disorientation angle between two grain (left) and Σ (right). The picture is taken from [6].

The current study is interested in inferring the constitutive model for GB diffusivity from the effective diffusivity of the polycrystals. To validate the inference method, a modified version of the BRK-energy model will be utilized because no general structure-property models for GB diffusivity currently exist, which will be explained further in Chapter 4.

2.2 Homogenization

The asymptotic method of homogenization is one rigorous averaging method in applied math which is commonly referred to as homogenization theory [38, 39]. The theory gives the macroscopic properties of materials, which contain two or more finely mixed substances (commonly known as composite materials), by viewing a composite material as a homogeneous material and considering its microscopic structure [40]. This theory has always been recognized as a powerful method to relate, as well as obtain, the effective properties of macroscopic materials with its structure-property model of heterogeneous microscopic substances [41–43].

Here, the method can also be applied to polycrystals because, in essence, a polycrystal is a solid macroscopic material containing two or more microscopic crystals/grains. Moreover, the effective properties of a material depend on its microstructural properties and spatial arrangement [44] and can be expressed as:

$$\bar{D} = H(M, D) \tag{2.2}$$

$\bar{D}$ is the effective property of the material (*i.e.* effective diffusivity in current study) and H is a homogenization relation containing microstructural information (M) and a structure-property model (D).

One early homogenization relation of diffusivity was proposed by Hart [45] in 1957. The Hart's model assumes that all GBs in polycrystals have the same value of diffusivity (in reality, each GB has different diffusivity measurement). Effective Medium Theory (EMT) [11, 46, 47] and percolation theory (percolation scaling laws) [48–53] are common homogenization relations that consider different diffusivity values for each GB. However, EMT is only accurate for the small range of GB diffusivity (GB low diffusivity contrast) and percolation theory only captures GB high diffusivity contrast. To capture both GB low and high contrast diffusivity, Chen and Schuh [11] applied the General Effective Medium (GEM) equation, developed by McLachlan [54, 55], which combine element of both EMT and percolation theory as a homogenization relation for GB diffusivity. The method, however, is challenging to be used to predict the effective diffusivity of general microstructures.

In this thesis, I utilize a more recent homogenization relation for GB diffusivity proposed by Johnson, Lund, and Critchfield [56] that considers the full spectrum of GB type; can be used with continuous and discrete constitutive models for GB diffusivity; and relatively easy to be used to predict the effective diffusivity of general microstructures. The method is utilizing the spectral graph theory (SGT) and will be called the SGT-method in this thesis. Using the SGT-method the effective diffusivity of the grain boundary network (GBN) can be calculated as [56]:

$$\bar{D}^{SGT}(\mathscr{D}, M) = \frac{L}{A}\left(\sum_{k>1} \lambda_k^{-1} \left(u_k(a) - u_k(b)\right)^2\right)^{-1} \tag{2.3}$$

where $\bar{D}^{\mathrm{SGT}}$ is the effective diffusivity predicted using the SGT-method; M abstractly represents the relevant microstructural information (*i.e.* the character and arrangement of the GBs in the present application); $\mathscr{D}$ is a function that abstractly represents the GB diffusivity structure-property model; L and A are the length and cross-sectional area of the polycrystal, respectively; λ_k is the k-th eigenvalue of the diffusivity-weighted GBN Laplacian matrix ($\mathscr{L}$), which encodes the topology of the GBN and the diffusivity of each GB; $u_k(a)$ and $u_k(b)$ are the a-th and b-th elements of

the k-th eigenvector of $\mathscr{L}$, where a and b are the indices of the diffusivity source and sink nodes respectively.

2.3 Property Localization

There are two common ways to employ Equation (2.2): $(\mathbf{1})$ to predict a material property where the microstructural information and the local property model are known; $(\mathbf{2})$ to design a material by solving for the microstructural information which need to be commensurate to the desired material property (the structure-property model is assure to be known). However, Equation (2.2) can also be used to infer a structure-property model when the effective property and the microstructural information are known. As the inverse of the homogenization relation, this approach of inferring constituent properties from the effective properties of a material is called property localization in this thesis. More specifically, the approach of inferring the constitutive model for GB property from the effective property of polycrystals will be referred to as GB property localization.

The GB property localization method was proposed by Johnson, Li, Demkowicz, and Schuh [34]. The property localization method presented by [34] was applied in an idealized two-dimensional honeycomb lattice. The diffusivity was assigned to GBs based on their disorientation utilizing the binary (low- and high-angle) method to define GBs type. The GEM was used as the homogenization relation, where the constitutive model for GB diffusivity was assumed to be a piecewise constant function of low- and high-angle diffusivity. In that prior work, GB property localization was performed by utilizing the least-squares function to obtain the parameters of the assumed structure-property model for GB diffusivity. As has also been mentioned, one major limitation of this method is that the form of GB structure-property model needs to be known *a priori* while for many GB properties, including diffusivity, the functional form of the structure-property model is the information one hopes to learn by the inference effort.

The goal of this study is to develop a new GB property localization method to infer the structure-property model for GB diffusivity from the effective diffusivity of polycrystals as a function of its all five crystallographic degrees of freedom without an *ansatz* for the model form. The property localization method presented in this thesis is applied to realistic two- and three-dimensional simulated polycrystals and the method to generate the polycrystals will be explained

further in Section 4.1. As has been explained in Section 2.2, this study employs the SGT-method as the homogenization relation relating the GB diffusivity and the effective diffusivity of the polycrystals. Further discussion of the development of the property localization and the validation of the method will be presented in Chapters 3 and 4.

CHAPTER 3. METHOD

Here I give a brief introduction to relevant aspects of inverse problem theory and then demonstrate its application to the problem of GB property localization. Additionally, the method to quantify the uncertainty of the inference is also presented here.

3.1 Inverse Problem Theory

Inverse problem theory is a method of inferring model parameters ($\mathbf{m}$) that characterize a system using the results of some measurements/observations of the system ($\mathbf{d}$) [57–61]. In a given system, $\mathbf{m} = \{m_1, m_2, \dots\}$ is a set containing the independent parameters and $\mathbf{d} = \{d_1, d_2, \dots\}$ is a set containing the dependent parameters, both of which we may only hope to know with some imperfect degree of certainty. Tarantola[1] proposed that our state of information (what we know about $\mathbf{d}$ and $\mathbf{m}$) can be described by a probability density function (PDF), called the *a posteriori* state of information, $\sigma(\mathbf{d},\mathbf{m})$, which is equal to the conjunction of the *a priori* state of information, $\rho(\mathbf{d},\mathbf{m})$, and the theoretical state of information, $\Theta(\mathbf{d},\mathbf{m})$ [57]. The *a priori* state of information is what we know before ever making any observations and may represent some known physical constraints. The theoretical state of information encodes correlations between $\mathbf{m}$ and $\mathbf{d}$ resulting from a homogenization or other physical theory and corresponding uncertainty. Using the Kolmogorov axioms, Tarantola and Valette showed that the *a posteriori* state of information is given by [58]:

$$\sigma(\mathbf{d},\mathbf{m}) = k\frac{\rho(\mathbf{d},\mathbf{m})\Theta(\mathbf{d},\mathbf{m})}{\mu(\mathbf{d},\mathbf{m})} \tag{3.1}$$

Here, k is a normalization constant, and $\mu(\mathbf{d},\mathbf{m})$ is the homogenous state of information, which is the PDF that assigns a probability to each region of the parameter space that is equal to the volume

[1] It is worth noting that a useful alternative Bayesian formulation of inverse problems exists, as described by [60,61], which results in a conditional *a posteriori* density $\sigma(\mathbf{m}\,|\,\mathbf{d})$. We have chosen to follow the approach introduced by Tarantola [57], which results in the joint *a posteriori* density $\sigma(\mathbf{d},\mathbf{m})$ and avoids the, perhaps rare, mathematical singularity that can exist in $\sigma(\mathbf{m}\,|\,\mathbf{d})$ for events with vanishing probability (Borel's paradox).

of that region [59]. In the present context, Equation (2.3) represents the forward problem. Thus, the observed effective diffusivity ($\bar{D}^{\text{obs}}$) is a dependent parameter and $\{\mathscr{D}, M\}$ are independent parameters. As will be described in Section 3.2, GB property localization typically leverages information from multiple samples, so that we have $\mathbf{M} = \{M_1, M_2, ..., M_N\}$ and $\bar{\mathbf{D}}^{\text{obs}} = \{\bar{D}_1^{\text{obs}}, \bar{D}_2^{\text{obs}}, ..., \bar{D}_N^{\text{obs}}\}$. Ignoring the normalization constant, we can then rewrite Equation (3.1) as:

$$\sigma(\bar{\mathbf{D}}^{\text{obs}}, \{\mathscr{D}, \mathbf{M}\}) \propto \frac{\rho(\bar{\mathbf{D}}^{\text{obs}}, \{\mathscr{D}, \mathbf{M}\})\Theta(\bar{\mathbf{D}}^{\text{obs}}, \{\mathscr{D}, \mathbf{M}\})}{\mu(\bar{\mathbf{D}}^{\text{obs}}, \{\mathscr{D}, \mathbf{M}\})} \tag{3.2}$$

The resolution of the inverse problem consists in identifying the structure-property model, $\mathscr{D}$, that is most probable given our observations of $\bar{D}^{\text{obs}}$ and M. This is accomplished by integrating Equation (3.2) to compute the *a posteriori* state of information over the space of independent parameters:

$$\sigma(\{\mathscr{D}, \mathbf{M}\}) = \int \sigma(\bar{\mathbf{D}}^{\text{obs}}, \{\mathscr{D}, \mathbf{M}\}) d(\bar{\mathbf{D}}^{\text{obs}}) \tag{3.3}$$

The evaluation of this integral is facilitated by considering relevant simplifications. Because the *a priori* information about $\mathbf{M}$ and $\mathscr{D}$ is not obtained from measurements of $\bar{D}^{\text{obs}}$, their states of information are independent [57], which implies that:

$$\rho(\bar{\mathbf{D}}^{\text{obs}}, \{\mathscr{D}, \mathbf{M}\}) = \rho(\bar{\mathbf{D}}^{\text{obs}})\rho(\{\mathscr{D}, \mathbf{M}\}) \tag{3.4}$$

$$\mu(\bar{\mathbf{D}}^{\text{obs}}, \{\mathscr{D}, \mathbf{M}\}) = \mu(\bar{\mathbf{D}}^{\text{obs}})\mu(\{\mathscr{D}, \mathbf{M}\}) \tag{3.5}$$

It should be noted here that $\rho(\bar{\mathbf{D}}^{\text{obs}})$ and $\rho(\{\mathscr{D}, \mathbf{M}\})$ are distinct functions. Conventional notation would include subscripts to distinguish them, such as $\rho_{\bar{\mathbf{D}}^{\text{obs}}}(\bar{\mathbf{D}}^{\text{obs}})$ and $\rho_{\{\mathscr{D}, \mathbf{M}\}}(\{\mathscr{D}, \mathbf{M}\})$, respectively. However, in the present case this becomes quite burdensome and difficult to read, so, for simplicity of notation, I omit the subscripts. I make explicit clarifications anywhere that context alone is insufficient to identify a particular function unambiguously.

I assume that Equation (2.3), as the physical theory relating the independent and dependent parameters, is at most mildly non-linear. Combining this assumption with the Kolmogorov definition for conditional probability [62], and taking the homogenous probability of the indepen-

dent parameters as their marginal probability, $\Theta(\bar{\mathbf{D}}^{\text{obs}}, \{\mathscr{D}, \mathbf{M}\})$ can be written, according to the treatment of Tarantola and Vallete [57, 58], as:

$$\Theta(\bar{\mathbf{D}}^{\text{obs}}, \{\mathscr{D}, \mathbf{M}\}) = \theta\left(\bar{\mathbf{D}}^{\text{obs}} \mid \{\mathscr{D}, \mathbf{M}\}\right) \mu\left(\{\mathscr{D}, \mathbf{M}\}\right) \tag{3.6}$$

Substituting Equations (3.2) and (3.4)–(3.6) into Equation (3.3), we obtain:

$$\sigma\left(\{\mathscr{D}, \mathbf{M}\}\right) \propto \rho\left(\{\mathscr{D}, \mathbf{M}\}\right) \int \frac{\rho(\bar{\mathbf{D}}^{\text{obs}}) \theta\left(\bar{\mathbf{D}}^{\text{obs}} \mid \{\mathscr{D}, \mathbf{M}\}\right)}{\mu(\bar{\mathbf{D}}^{\text{obs}})} d(\bar{\mathbf{D}}^{\text{obs}}) \tag{3.7}$$

Because the manifold that $\bar{\mathbf{D}}^{\text{obs}}$ inhabits is a linear space, using the definition of homogenous probability distribution presented by Mosegaard and Tarantola [59], I conclude that $\mu(\bar{\mathbf{D}}^{\text{obs}})$ is constant. I also make the simplifying approximation that any uncertainty in Equation (2.3) is negligible, which implies that $\theta\left(\bar{\mathbf{D}}^{\text{obs}} \mid \{\mathscr{D}, \mathbf{M}\}\right) = \delta(\bar{\mathbf{D}}^{\text{obs}} - \bar{\mathbf{D}}^{\text{SGT}}(\mathscr{D}, \mathbf{M}))$. Under these conditions, the integration operation in Equation (3.7) results in:

$$\sigma(\{\mathscr{D}, \mathbf{M}\}) \propto \rho\left(\{\mathscr{D}, \mathbf{M}\}\right) \rho\left(\bar{\mathbf{D}}^{\text{SGT}}(\mathscr{D}, \mathbf{M})\right) \tag{3.8}$$

The last term, $\rho\left(\bar{\mathbf{D}}^{\text{SGT}}(\mathscr{D}, \mathbf{M})\right) = \rho_{\bar{\mathbf{D}}^{\text{obs}}}\left(\bar{\mathbf{D}}^{\text{SGT}}(\mathscr{D}, \mathbf{M})\right)$, is a likelihood function, which quantifies how well the model explains the data. In other words, $\rho\left(\bar{\mathbf{D}}^{\text{SGT}}(\mathscr{D}, \mathbf{M})\right)$ quantifies how well the independent parameters explain the dependent parameters. Thus, the *a posteriori* state of information about the independent parameters is proportional to the product of the likelihood function and the *a priori* state of information about the independent parameters.

3.2 GB Property Localization

In this section, I describe how GB property localization is done in general, and then how the inverse problem theory discussed in the previous section may be applied in this context. GB property localization [34] consists of first characterizing the microstructures of a set of polycrystals, *e.g.*, via Electron Back-Scatter Diffraction (EBSD). The resulting microstructural information is denoted $\mathbf{M} = \{M_1, M_2, ..., M_N\}$, where M_i describes the i-th microstructure. Measurements are then performed to determine the relevant effective property of each polycrystal. In the present case I am interested in the effective diffusivity, $\bar{\mathbf{D}}^{\text{obs}} = \{\bar{D}_1^{\text{obs}}, \bar{D}_2^{\text{obs}}, ..., \bar{D}_N^{\text{obs}}\}$. The relevant homogeniza-

tion relation, Equation (2.3), is then inverted to determine the unknown structure-property model, $\mathscr{D}$.

Here, I propose the use of inverse problem theory to perform the homogenization inversion step to solve for the unknown structure-property model. With $\mathbf{M}$ and $\bar{\mathbf{D}}^{\text{obs}}$ obtained via measurement, I solve for the unknown structure-property model for GB diffusivity ($\mathscr{D}$) by determining, among all possible models, the one that maximizes the *a posteriori* probability density $\sigma(\{\mathscr{D},\mathbf{M}\})$. I wish to do this without an *ansatz* for the model form, so that both the form and any model parameters are dictated by the observed data. As will be described below, I accomplish this by first discretizing the domain of $\mathscr{D}$, then describing the *a priori* state of information by appropriate PDFs, and finally, solving an optimization problem with Equation (3.8) as the objective function to infer the value of the diffusivity structure-property model in each bin, thus obtaining a discrete approximation to $\mathscr{D}$.

Because I wish to infer the structure-property model without *a priori* knowledge of its form, I discretize the GB character space so that $\mathscr{D}$ will be approximated as a piecewise-constant function with unknown parameters $\mathbf{D} = \{D_1, D_2, ..., D_J\}$, where D_j is the diffusivity of a GB whose crystallographic character inhabits the j-th bin and J is the total number of bins. The only *a priori* information about the model parameters that I consider is that the diffusivity is everywhere non-negative (*i.e.* I assume that no spinodal-type phase transformation is occurring). The *a priori* information about $\mathbf{D}$ can then be represented as a Heaviside step function:

$$\rho(\mathbf{D}) = \begin{cases} 1, & D_j \geq 0, \forall\ j \in [1,J] \\ 0, & \text{otherwise} \end{cases} \tag{3.9}$$

Because I am using simulated polycrystals, my *a priori* knowledge of each microstructure is exact. Consequently, I utilize an indicator function to represent the *a priori* state of information about $\mathbf{M}$:

$$\rho(\mathbf{M}) = \begin{cases} 1, & M_i = M_i^{\text{act}}, \forall\ i \in [1,N] \\ 0, & \text{otherwise} \end{cases} \tag{3.10}$$

where M_i^{act} is the actual state of the i-th microstructure. If experimental samples were considered, their characterization would be inexact and the indicator function would be replaced with a distribution whose dispersion encoded the uncertainty resulting from the characterization procedure. We have hitherto referred abstractly to $\mathbf{M}$ as containing some information about the state of the microstructure. This is because for property localization in general, different properties of interest may depend on the character/state of different microstructural features (e.g. composition, phase fractions, phase morphology, crystallographic texture). The details about what information is contained in $\mathbf{M}$ and how it is represented are therefore problem specific, but the methods presented here are quite general. For the present problem, $\mathbf{M}$ contains the character and arrangement of the GBs in the microstructure, as explicitly given by the GBN Laplacian, $\mathscr{L}$.

The independence of $\mathbf{D}$ and $\mathbf{M}$ implies that their joint distribution is given by:

$$\rho\left(\{\mathbf{D},\mathbf{M}\}\right) = \rho(\mathbf{D})\rho(\mathbf{M}) \tag{3.11}$$

Finally, for each polycrystal, I represent the likelihood function by a Gaussian-like PDF:

$$\rho\left(\bar{D}^{\text{SGT}}(\mathbf{D},M_i)\right) \propto \exp\left(-\frac{\left(\bar{D}_i^{\text{obs}} - \bar{D}^{\text{SGT}}(\mathbf{D},M_i)\right)^2}{2s_i^2}\right) \tag{3.12}$$

where, s_i characterizes the measurement uncertainty of $\bar{D}_i^{\text{obs}}$. Considering all of the microstructures together we have, again because of independence, the joint distribution

$$\rho\left(\bar{\mathbf{D}}^{\text{SGT}}(\mathbf{D},\mathbf{M})\right) \propto \exp\left(-\sum_{i=1}^{N}\frac{\left(\bar{D}_i^{\text{obs}} - \bar{D}^{\text{SGT}}(\mathbf{D},M_i)\right)^2}{2s_i^2}\right) \tag{3.13}$$

This implies that when a model ($\mathbf{D}$) is considered that minimizes the difference between $\bar{\mathbf{D}}^{\text{obs}}$ and $\bar{\mathbf{D}}^{\text{SGT}}(\mathbf{D},\mathbf{M})$, the likelihood will be maximized and such a model would best explain the observed data.

Substituting Equations (3.11) and (3.13) into Equation (3.8), we obtain for the *a posteriori* state of information for the independent parameters:

$$\sigma\left(\{\mathbf{D},\mathbf{M}\}\right) \propto \begin{cases} \exp\left(-\sum_{i=1}^{N} \frac{\left(\bar{D}_i^{\text{obs}} - \bar{D}^{\text{SGT}}(\mathbf{D},M_i)\right)^2}{2s_i^2}\right), & \mathbf{M}=\mathbf{M}^{\text{act}}, \mathbf{D}\geq 0 \\ 0, & \text{otherwise} \end{cases} \tag{3.14}$$

With an expression for the *a posteriori* state of information in hand we are now in a position to perform the inversion of the homogenization equation to infer a discrete approximation to $\mathscr{D}$. This is accomplished by maximizing $\sigma\left(\{\mathbf{D},\mathbf{M}\}\right)$, with the D_j as the design variables:

$$\underset{\mathbf{D}}{\text{argmax}}\, \sigma\left(\{\mathbf{D},\mathbf{M}\}\right) \tag{3.15}$$

To facilitate the optimization process, I make two adjustments to the problem. First, because GB diffusivities can span many orders of magnitude, I rescale the optimization problem logarithmically. Second, to improve convergence of the optimization algorithms we employ, I smooth out $\sigma\left(\{\mathbf{D},\mathbf{M}\}\right)$ by conservativelly approximating $s_i \approx s \equiv \max(s_i)$. Applying these two adjustments, our optimization problem becomes:

$$\begin{aligned} \underset{\log(\mathbf{D})}{\text{argmax}} \quad & \exp\left(-\sum_{i=1}^{N} \frac{1}{2s^2}\left(\bar{D}_i^{\text{obs}} - \bar{D}^{\text{SGT}}(\mathbf{D},M_i)\right)^2\right) \\ \text{subject to} \quad & \mathbf{M}=\mathbf{M}^{\text{act}} \\ & \mathbf{D}\geq 0 \end{aligned} \tag{3.16}$$

I have observed $\sigma\left(\{\mathbf{D},\mathbf{M}\}\right)$ to be nearly flat everywhere except in a small region close to the optimum, making convergence challenging. To address this, I perform the optimization in two stages. In the first pass, I maximize $\log\left[\sigma\left(\{\mathbf{D},\mathbf{M}\}\right)\right]$ to get close to the region containing the optimum. Then, in the second pass, I finish the optimization process by maximizing $\sigma\left(\{\mathbf{D},\mathbf{M}\}\right)$. For the first pass, I use MATLAB's `fmincon()` function [63]. For the second pass, I employ the Nelder-Mead Simplex algorithm [64], as implemented in the `fminsearcbnd()` function written by John D'Erico [65].

Solution of Equation (3.16) allows us to infer the unknown structure-property model for GB diffusivity without knowing the form of the model *a priori*. Additionally, because the *a pos-*

teriori information is represented by a probability density function, it is possible to quantify the uncertainty of the inference [60, 61], as will be explained further in Section 3.3.

3.3 Uncertainty Quantification

In addition to inferring the structure-property model that is most probable given the observed data, it is also desirable to quantify how much uncertainty exists in our inferred result (see [60, 61]). In technical terms, I seek to quantify the dispersion in the *a posteriori* state of information about the independent parameters, $\sigma(\{\mathbf{D},\mathbf{M}\})$, resulting from the combined influence of the dispersion in all of the underlying models of the *a priori* states of information (including limitations due to measurement resolution). Here I make these ideas concrete and describe how I calculate the uncertainty before presenting the inference results, together with their corresponding uncertainty.

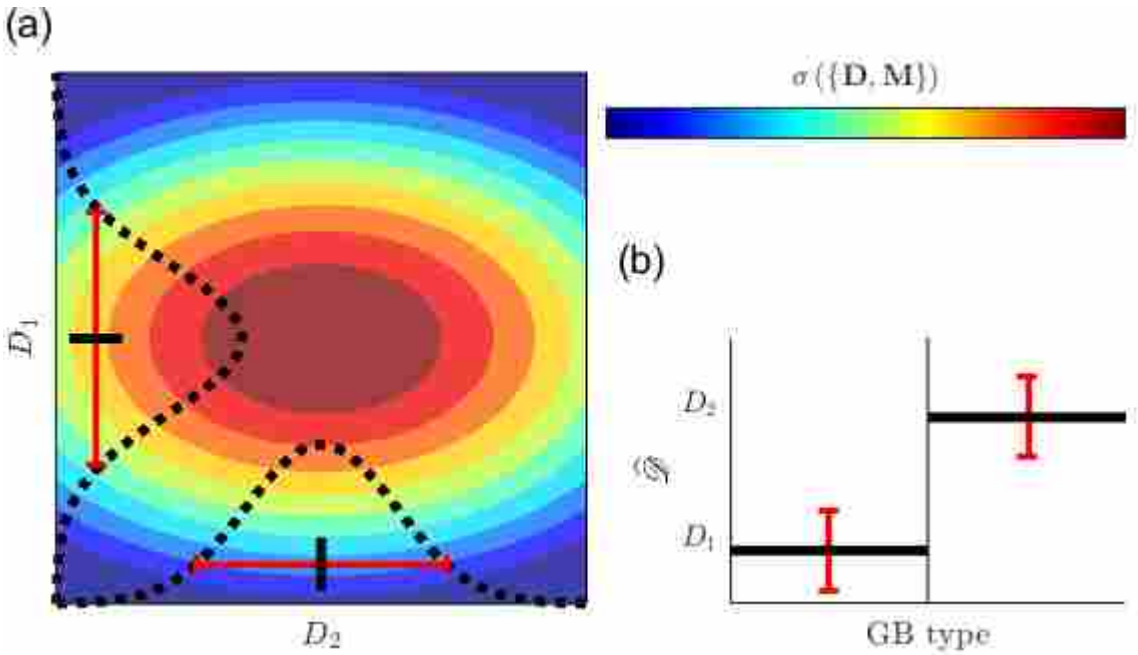

Figure 3.1: Illustration of the uncertainty quantification method. (a) Contour plot of $\sigma(\{\mathbf{D},\mathbf{M}\})$ with the marginal densities for each dimension shown as dotted lines. (b) The corresponding structure-property model ($\mathscr{D}$), discretized into two bins.

Let us consider a simple example in which the domain of the structure-property model ($\mathscr{D}$) is discretized into only two bins (see Figure 3.1b). For this example, the domain of $\sigma(\{\mathbf{D},\mathbf{M}\})$ is two dimensional, so we can directly visualize it as the contour plot shown in Figure 3.1a. Each point in the space shown in Figure 3.1a represents a different candidate structure-property model, whose coordinates are the elements of $\mathbf{D}$ and provide the values of the structure-property model in each bin. The color of the contour plot represents the value of $\sigma(\{\mathbf{D},\mathbf{M}\})$, which represents the probability (density) that any structure-property model is consistent with the observed data, taking into account relevant uncertainties. Thus the model associated with the peak in Figure 3.1a is the one that is most consistent with the observed data. The marginal density in each dimension (shown as dotted black lines in Figure 3.1a) provides a measure of the uncertainty of the inferred value in the corresponding bin. From the marginal distributions, confidence intervals can be calculated, and these are used in our graphical representations of uncertainty.

Accurate inference of $\mathscr{D}$ requires the use of more than two bins and because the dimensionality of the problem is equal to the number of bins employed, which may be large, calculation of the marginal distributions requires some care. Estimation of the marginal densities from uniform sampling of $\sigma(\{\mathbf{D},\mathbf{M}\})$ is straightforward, but computationally expensive for high dimensional problems. Consequently, I employ the following procedure. I first sample the space around the optimum model using the Metropolis-Hastings algorithm (as implemented in the `mhsample()` function in MATLAB [63]), with $\sigma(\{\mathbf{D},\mathbf{M}\})$ as the target distribution. Then, the marginal densities are estimated from the resulting samples via the linear diffusion based Kernel Density Estimation (KDE) method of Botev, Grotowski, and Kroese [66] (see [67] for a MATLAB implementation). With the estimated marginal density in each bin, I can then calculate the confidence interval for the inferred value of each D_j.

CHAPTER 4. VALIDATION

As has been mentioned, GB Property Localization consists of first characterizing the microstructures of a set of polycrystals, determining the relevant effective property of each polycrystal, and finally inferring the unknown structure-property model. Because no general structure-property models for GB diffusivity currently exist, the validation of the method developed in this thesis is done in a hypothetical case as follows. First, the two- and three-dimensional synthetic polycrystals are generated using the method in Section 4.1. Then, for each microstructure, the effective diffusivity is calculated using the SGT method where the GB diffusivity value in the GBN is assigned using a hypothetical constitutive model as will be explained further in Section 4.2. And finally, validation of the inference method then consists of comparing the "actual" constitutive model (assign in Section 4.2) with the inference result.

4.1 Microstructures Generation

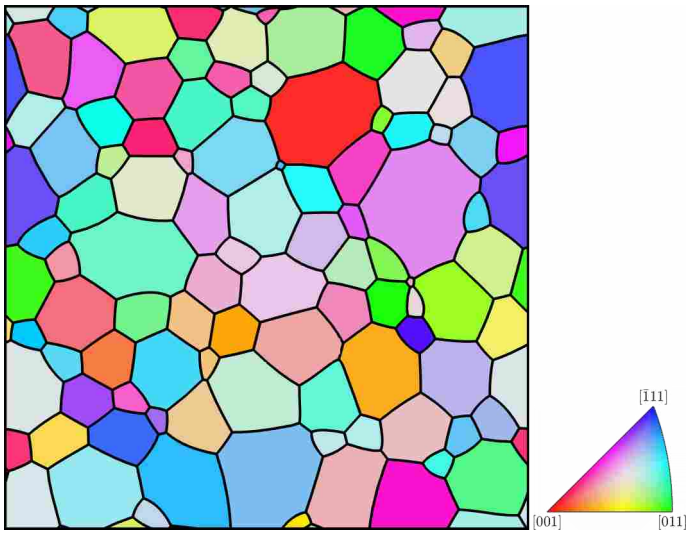

Figure 4.1: Example of a two-dimensional polycrystal template used in this study. Colors indicate crystallographic orientation, as shown in the accompanying inverse pole figure (IPF) color legend.

In an effort to validate the method, two- and three-dimensional polycrystals are generated. The two-dimensional polycrystalline microstructures are generated using the method of [56]. Each microstructure is the result of an isotropic grain growth simulation performed using a front-tracking algorithm [68] (code written by Jeremy Mason[1]). Each simulation was initialized with a Voronoi microstructure constructed from randomly generated uniformly distributed seeds and resulting in 1000 cells (*i.e.* grain precursors). The simulations allowed the microstructure to evolve under mean curvature flow until about 100 grains remain. Then grain orientations are assigned according to the simulated annealing procedure described in [56] which ensures that the generated polycrystals span the space of possible triple-junction fractions[2] in order to encourage diversity of the GBN structure in the resulting set of microstructures. An example microstructure generated by this procedure is shown in Figure 4.1. A pool of 1771 polycrystals was generated, from which representatives were randomly selected during the inference process.

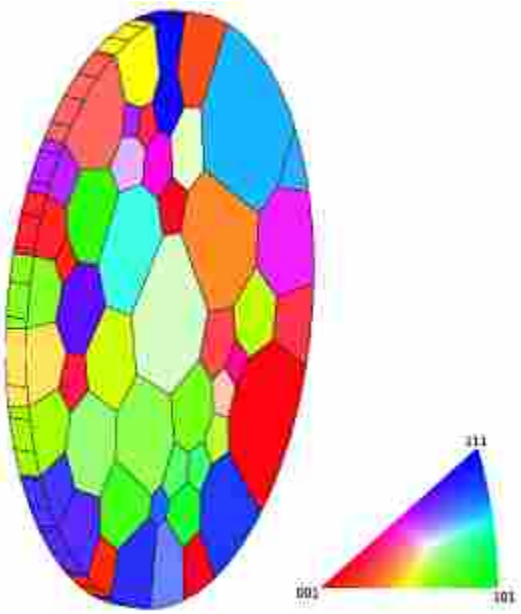

Figure 4.2: Example of a three-dimensional polycrystal template used in this study with crystallographic orientation is represented using IPF coloring.

[1]The code implements the method established by [68], and is available at `http://web.boun.edu.tr/jeremy.mason/documents/FTGG2_v1_0.zip`.

[2]Triple junction fractions, J_0, J_1, J_2, and J_3, represent the population of GB triple junctions coordinated by $0, 1, 2$, or 3 "special" GBs, respectively. Further discussion about triple junction fractions can be found in [69–74].

I generated a pool of 2000 three-dimensional polycrystals in coined geometry using Neper software version 3.0.2 [75–78] (see Figure 4.2), from which representatives were also randomly selected during the inference process. Each polycrytal is constructed using the grain growth algorithm (`-morpho gg`) available in `neper -T` module [76, 78] where I set the simulation to stop when there are 50 grains left (`-n 50`). `-oricrysym cubic` and `-domain "cylinder(0.1,1)"` options are used to create polycrystals with cubic crystal symmetry in coined shape geometry. In order to use the SGT method to calculate the effective diffusivity of the polycrystals, `-dim 2` and `-mesh2dalgo fron` options from `neper -M` module are used to mesh the GBs of the polycrystals using frontal meshing algorithm resulting in a nearly orthogonal triangular mesh. The grain orientations are then assigned from uniformly distributed random orientations.

4.2 Obtaining Effective Diffusivity

The next step is to obtain the effective diffusivity data. To do this, I calculated the effective diffusivity for each polycrystal using Equation (2.3). For our synthetic microstructures, Equation (2.3) is exact. However, in practical applications, one would employ digital representations of microstructures acquired from, *e.g.*, EBSD measurements, and property measurement techniques with finite resolution. To simulate uncertainties that would arise from the approximate nature of such digital representations as well as resolution limitations and measurement uncertainty, I add Gaussian noise[3], $\varepsilon \sim N\left[0, \left(19\% \left(\bar{D}^{\mathrm{SGT}}\right)\right)^2\right]$, such that the observed effective diffusivity $(\bar{D}^{\mathrm{obs}})$ is given by:

$$\bar{D}^{\mathrm{obs}} = \bar{D}^{\mathrm{SGT}} + \varepsilon \tag{4.1}$$

In this present case, s_i in Equation (3.14) is equal to the standard deviation of the noise I introduced (*i.e.* $19\%\bar{D}^{\mathrm{SGT}}(\mathbf{D}, M_i)$). Because I assume that I have only $\bar{\mathbf{D}}^{\mathrm{obs}}$ data, I estimate the value of s_i by taking $19\% \left(\bar{D}_i^{\mathrm{obs}}\right)$ as the value of s_i.

With both $\bar{D}^{\mathrm{obs}}$ and M being measured, the unknown in Equation (2.3) is the structure-property model, $\mathscr{D}$, which we seek to infer using the tools of inverse problem theory. For the purposes of validation, I assign GB diffusivities using a hypothetical constitutive model. Because

[3]The value of the standard deviation here is similar to that observed for effective diffusivity measurements of solution annealed 465 stainless steel reported by [79].

no general structure-property models for GB diffusivity currently exist[4], I employ the function developed by Bulatov, Reed, and Kumar to describe GB energy [23], but I map it to the range of realistic values of GB diffusivity as described later; I will refer to this as the BRK model. With GB diffusivities assigned, I then calculate the effective diffusivity using the procedure already described, including the introduction of noise. During the inference process, I ignore any knowledge of the assigned constitutive model and consider only M and $\bar{D}^{\text{obs}}$ as the input variables.

4.3 Inferring and Validating

I considered one-, three-, and five-dimensional constitutive models to validate the inference method. In the first case, I considered two-dimensional microstructures in which the crystallographic orientations of all grains shared a common $\langle 100 \rangle$ axis and all GBs were of $\langle 100 \rangle$ tilt character where the GB plane is ignored so that $\mathscr{D}$ was a one-dimensional function of ω. I refer to this as the one degree-of-freedom (1DOF) case. In the second case, I considered more general two-dimensional microstructures with arbitrary crystallographic orientations resulting in arbitrary disorientations, but I again ignored the influence of the GB plane so that $\mathscr{D}$ was a three-dimensional function of the angle (ω) and axis (θ, ϕ) of the disorientation. I refer to this as the three degree-of-freedom (3DOF) case. For the final case, I considered three-dimensional microstructures with arbitrary disorientation and GB plane so that $\mathscr{D}$ was a five-dimensional function of the disorientation angle (ω), rotation axis (θ, ϕ), and the normal of the GB plane (α, β). I refer to this as the five degree-of-freedom (5DOF) case.

To validate the method, I first characterized the simulated polycrystals to obtain the microstructural information $(\mathbf{M})$. Then, I obtained the observed effective diffusivity $\bar{\mathbf{D}}^{\text{obs}}$ of the polycrystals by means of the method presented in Section 4.2. I then employed the proposed GB property localization method to infer $\mathscr{D}$ without considering any prior information about the true underlying structure-property model. Validation of the inference method was then carried out by comparing the true constitutive model with the inference result. To aid with convergence of the stochastic optimization, I performed the localization process 50 times for each constitutive model and kept the result with the highest value of $\sigma(\{\mathbf{D}, \mathbf{M}\})$. For each inference attempt, $\mathbf{M}$ was com-

[4] In the absence of a measured structure-property model, computational studies have typically employed a binary step-function [11, 34], though there are some examples of continuous functions [80].

posed of 100 randomly selected microstructures from the respective pools of 1771 two-dimensional or 2000 three-dimensional simulated polycrystals.

CHAPTER 5. RESULTS AND DISCUSSION

5.1 Validation Results

Here I present the inference results first before discussing the important aspects of it. The results will be presented case by case to make a clear comparison, starting with the 1DOF case.

5.1.1 1 DOF Validation Results

As mentioned previously, the discretization produces a piecewise-constant approximation to $\mathscr{D}$, which I will denote $\widehat{\mathscr{D}}$. In the 1DOF case, we have:

$$\widehat{\mathscr{D}}(\omega) = \begin{cases} D_1, & 0 < \omega \leq b_1 \\ D_2, & b_1 < \omega \leq b_2 \\ . & . \\ . & . \\ . & . \\ D_J, & b_{J-1} < \omega \leq b_J \end{cases} \tag{5.1}$$

where, D_j is the diffusivity of the j-th bin; J is the total number of bins; and b_j is the upper limit of the j-th bin. I employed a uniform discretization with 4.5° resolution so that $b_j = (4.5j)^\circ$. I considered two different constitutive models for the 1DOF validation tests.

The first 1DOF constitutive model, as mentioned previously, was a modified version of the BRK model [23], which I linearly scaled and shifted to the range of realistic values of GB diffusivity for aluminum. Specifically, this transformation resulted in a model for which the minimum and maximum GB diffusivities were equal to those employed in [81], which were extracted from the atomistic calculations of [82]. The second 1DOF test employed the following analytical model:

$$\mathscr{D}(\omega) = D_{\text{high}} \exp\left(\left(\log\left(\frac{D_{\text{low}}}{D_{\text{high}}}\right)\right)\left(\left(\frac{4\omega}{\pi}\right) - 1\right)^4\right) \tag{5.2}$$

which is similar in form to results from experimental and computational surveys of diffusivity for $\langle 100 \rangle$ tilt GBs [82, 83]. In Equation (5.2), D_{low} and D_{high} are the minimum and maximum diffusivities respectively, the values of which were the same as those employed in the 1DOF BRK model.

There are several things to note about the constitutive models employed here. First, there is no existing structure-property model to predict GB diffusivity as a function of GB crystallography. Consequently, the models I have employed are not intended to be quantitatively accurate descriptions of actual GB diffusion processes, rather I have chosen models that possess qualitative features (e.g. the existence of singularities, diffusivity values that vary over many orders of magnitude) that reflect trends observed in the literature, in order to assess how well such features can be captured by the localization technique. Second, for the 1DOF case, the grain orientations assigned to the simulated polycrystal share a common $\langle 100 \rangle$ rotation axis orthogonal to the sample surface, making all of the GBs $\langle 100 \rangle$ tilts. The first model I employed for $\mathscr{D}(\omega)$ is constructed by evaluating the full five degree-of-freedom BRK model over the one-dimensional submanifold corresponding to $\langle 100 \rangle$ symmetric tilt GBs. The data that inspired the second 1DOF model were also for $\langle 100 \rangle$ symmetric tilt GBs. Although all of the GBs in the 1DOF simulated microstructures are strictly $\langle 100 \rangle$ tilts, they are not actually all symmetric tilts, and, to make the model one-dimensional, I have ignored the GB plane altogether. Because I have ignored the GB plane, the domain of the disorientation angle is symmetric about 45°. Again, fidelity to the crystallography of the original data that inspired the models was not the objective. Rather, regardless of their origin, I have selected/constructed models whose forms exhibit relevant features.

The localization results for both models, together with the quantified uncertainty, can be seen in Figure 5.1, where the green line is the model we attempted to infer (and which was ignored during the inference process). The red line represents the piece-wise constant inference, which is the most probable model given the observations. The gray area represents the 95% confidence interval, which is my chosen metric to represent the uncertainty. Finally, the histogram shows the disorientation angle distribution across all of the microstructures employed in the inference.

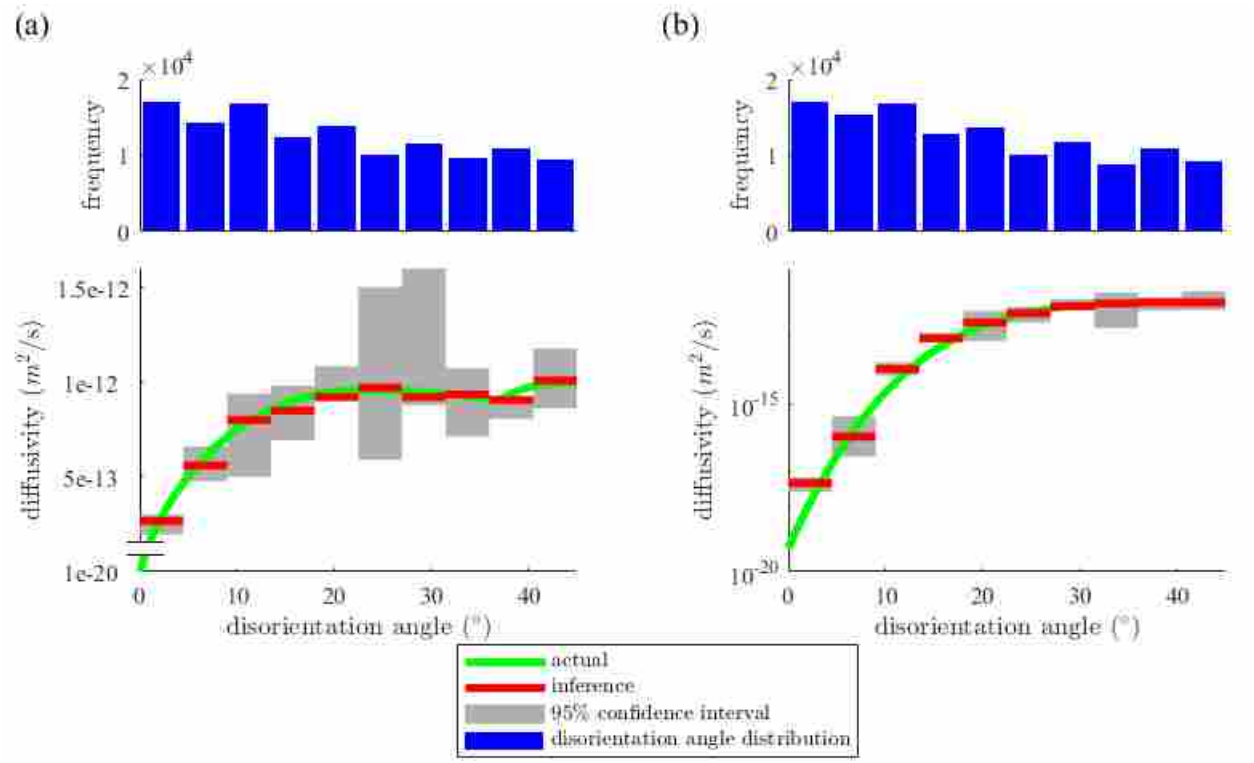

Figure 5.1: Comparison between the inferred model and the true model for (a) the 1DOF BRK function and (b) the exponential function of Equation (5.2), together with quantified inference uncertainty. The disorientation angle distribution across all of the employed microstructures is shown in histogram form above each plot.

Note that with 100 randomly selected microstructures all of the bins contain a multiplicity of observations. Even with the coarse binning, and piece-wise constant representation, the results show very good agreement with the true models in both cases. In particular, we can note that the localization inference successfully captured the singularity in the 1DOF BRK model (Figure 5.1a). A quantitative discussion of the inference accuracy is presented later. Figure 5.1b confirms that the method is also successful when the constitutive model spans many orders of magnitude. The uncertainty in this test appears smaller, due to the logarithmic scale of Figure 5.1b, but it is actually similar in magnitude to the uncertainty in Figure 5.1a.

5.1.2 3 DOF Validation Result

For the 3DOF case, the GB property localization approach was validated against another modified version of the BRK-energy function. In this case, instead of evaluating the BRK model

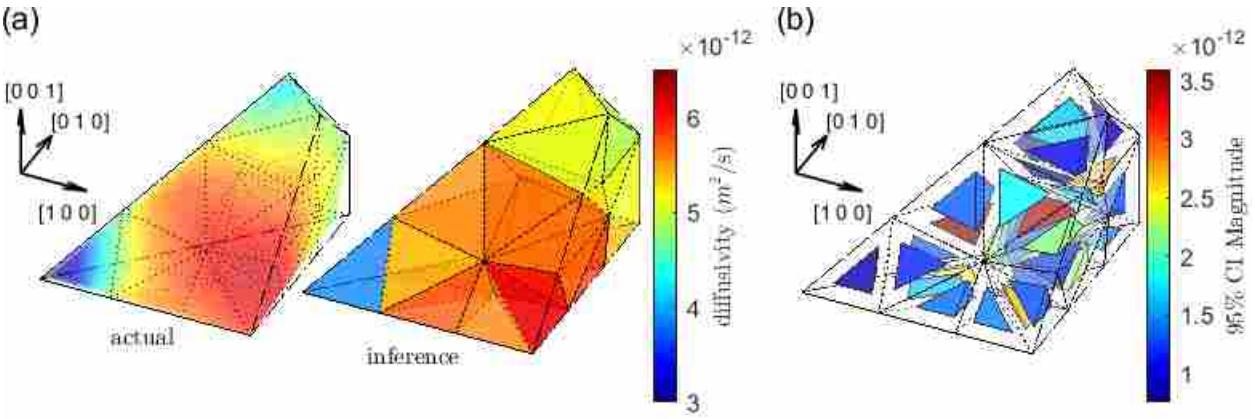

Figure 5.2: (a) Comparison between the true (left) and the inferred (right) 3DOF GB diffusivity structure-property model, displayed in the Rodriguez space parameterization of the disorientation FZ. (b) The magnitude of the 95% confidence interval for the inference in each bin (a measure of the uncertainty in the inference). Interior lines define the boundaries of the tetrahedral bins. To facilitate visualization of the uncertainty in the interior of the FZ, the tetrahedral bins are slightly reduced in size in (b).

along a submanifold, a three-dimensional constitutive model was constructed by integrating over the degrees of freedom corresponding to the GB plane:

$$\mathscr{D}(\omega,\theta,\phi) \propto \int_0^{2\pi} \int_0^{\frac{\pi}{2}} \mathrm{BRK}(\omega,\theta,\phi,\alpha,\beta)\sin\alpha \,\mathrm{d}\alpha \,\mathrm{d}\beta \tag{5.3}$$

In this 3DOF GB structure-property model, the diffusivity is a function of the disorientation angle (ω) and axis (θ,ϕ). Discretization of the disorientation FZ was carried out using the volumetric meshing capabilities of the Neper software package [75–78] with the Rodriguez space parameterization of the disorientation FZ supplied as the domain. The `-mesh3dalgo netg:gmne` meshing option was employed, which resulted in bins of approximately equal volume (see Figure 5.2).

Figure 5.2a shows the results of the localization inference applied to the 3DOF model, using a total of 33 bins. Figure 5.2b shows the uncertainty of the inference as represented by the magnitude of the 95% confidence interval for each bin, which, we note, are similar in magnitude to the uncertainty in the 1DOF case. The 3DOF case shows that with a relatively coarse discretization, the GB property localization approach gives a satisfactory approximation to the constitutive model (see Figure 5.2a), though this is admittedly problem specific and is likely to depend on how smooth the underlying constitutive model is. This case is a nice test to confirm that the localization method

can be applied to a higher dimensional model before applying it to infer a structure-property model for GB diffusivity with all five degrees of freedom.

5.1.3 5 DOF Validation Result

The 5DOF validation utilized the BRK model with all five degrees of freedom [23], which I linearly scaled and shifted to the range of GB diffusivity for aluminum employed in [81]. Discretization of the disorientation FZ was carried out using the same method used in 3DOF case into 19 bins. Each point in the disorientation FZ possesses a hemisphere space of the GB plane FZ. I discretized the GB plane FZ by generating approximately uniformly spaced points on the hemisphere using the `GridSphere()` function written by Kurt Von Laven [84] using 10 bins. The product space of the disorientation FZ (19 bins) and GB plane FZ (10 bins) contained in total 190 bins over five-dimensional space. For this test, I was considering the case where I introduced $\varepsilon = 0$ noise to Equation (4.1).

Figure 5.3 shows the results of the localization inference applied to the 5DOF model. The big circles are the stereographic projections of the hemisphere space which corresponds to a specific points in the disorientation FZ space as shown by the label on top of each hemisphere. The color of the hemisphere surface represents the diffusivity value calculated using the true constitutive model. The small circular markers are the center of each bin in the hemisphere space with the color representing the diffusivity value calculated using the inferred constitutive model. The result shows that the GB property localization approach gives a satisfactory approximation to the true constitutive model at most of the regions in the 5DOF domain. However, there are some regions with noticeable error even with no observation noise (see Figure 5.3). A further analysis will be discussed in Section 5.2 to determine the accuracy of the GB property localization approach in 5DOF case. Although visually there are still some regions whth imperfect inference, the result is still encouraging because the approach gives a satisfactory approximation at most of the regions.

Figure 5.4 shows the magnitude of the 95% confidence interval for the inference. It is notable that the magnitude of the uncertainty is still similar to the uncertainty in the 1DOF and 3DOF cases.

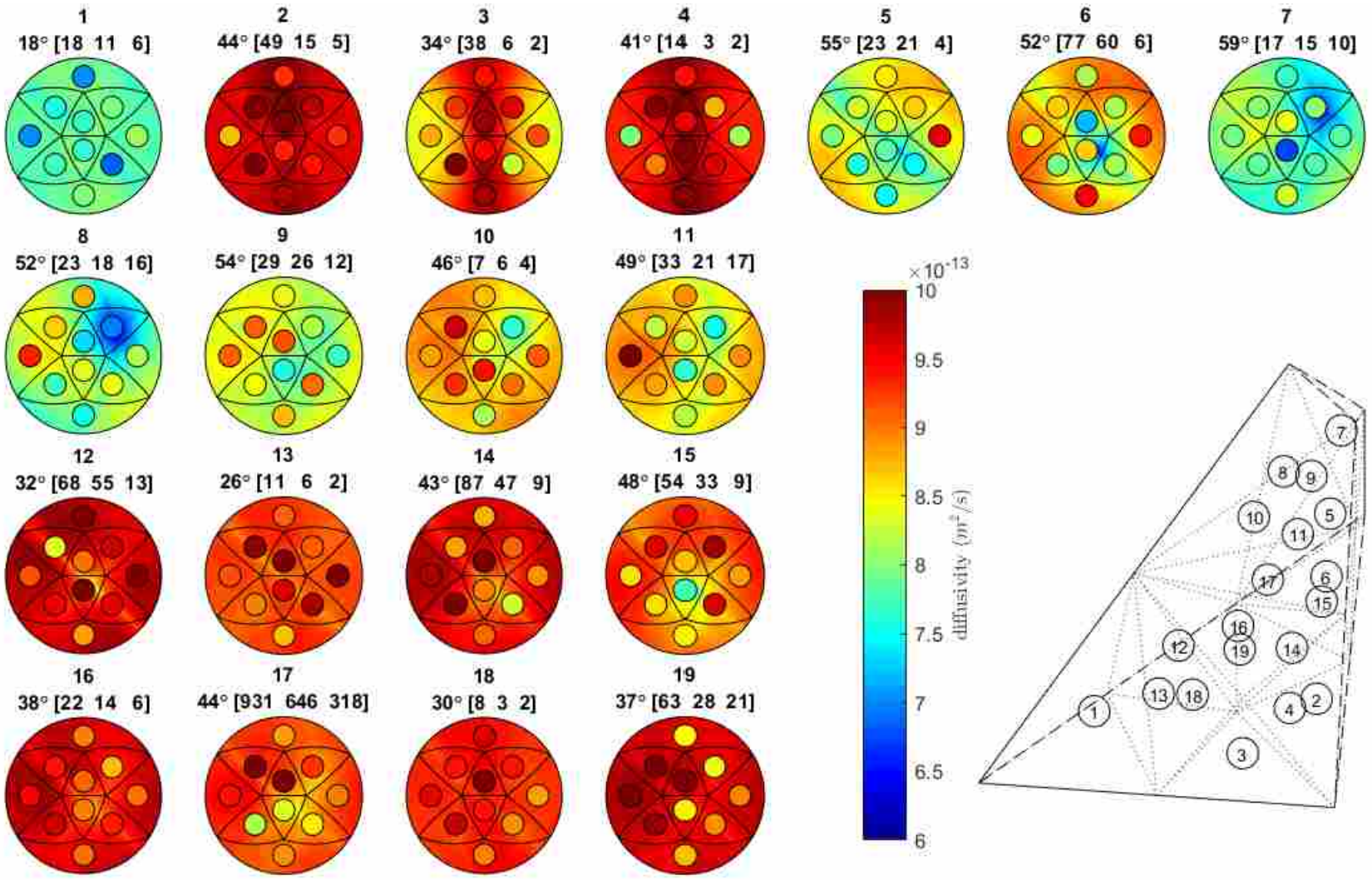

Figure 5.3: Comparison between the true and the inferred 5DOF GB diffusivity structure-property model. Each big circle is the stereographic projection of the hemisphere (GB plane FZ) corresponding to the center of the bin in the disorientation FZ, displayed in the Rodriguez space, which is specified by the numbering of the point. The color of the hemisphere represents the true diffusivity value and the small circular markers indicate the inferred diffusivity value in each bin using the same color scale.

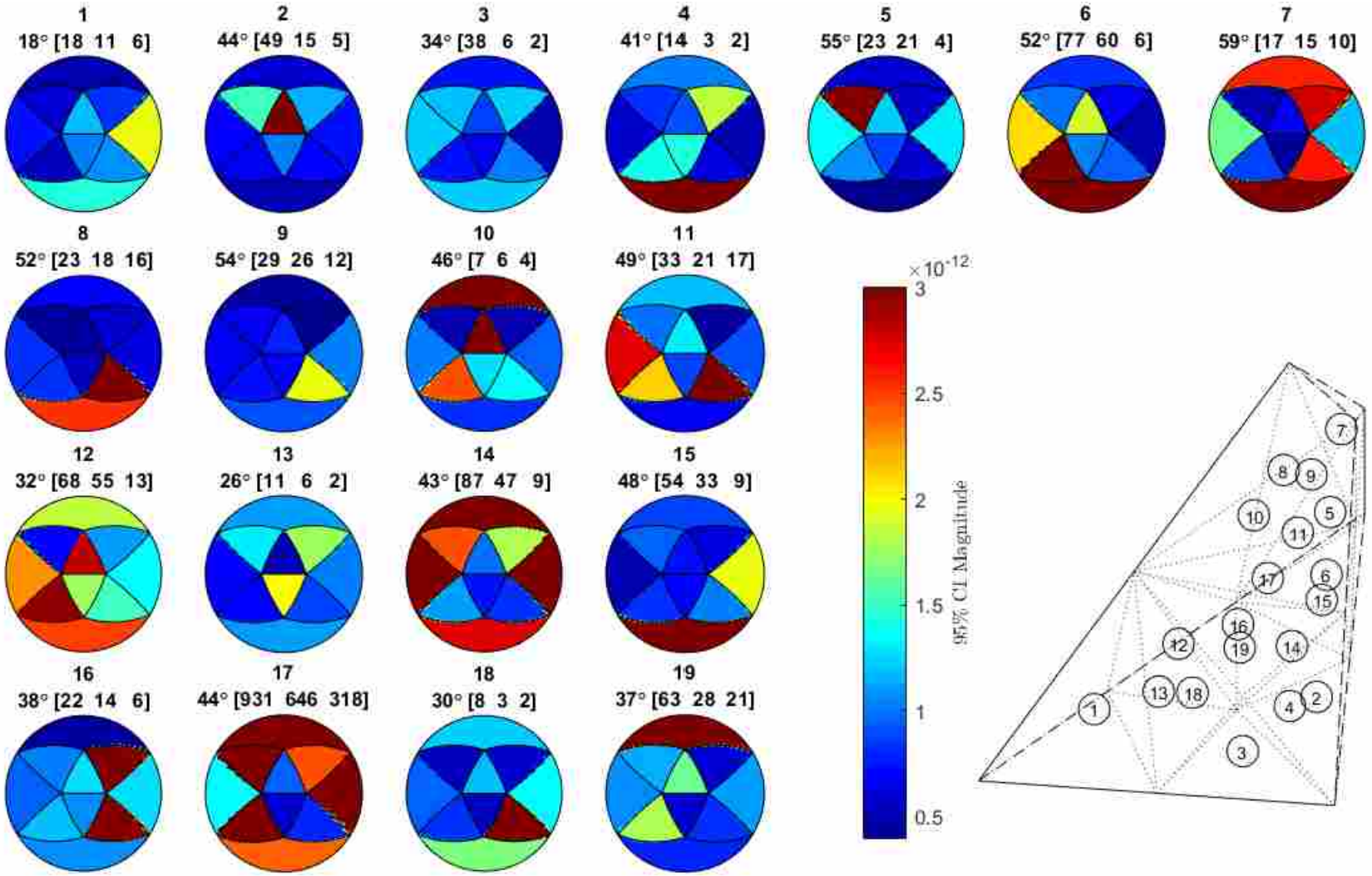

Figure 5.4: Plots of the 95% confidence interval's magnitude for the inference in each bin (a measure of the uncertainty in the inference) shown as the color of the hemisphere with accompanying colormap.

5.2 Discussion

The results just described demonstrate that the inverse problem theory approach to GB property localization can successfully infer a discrete approximation to an unknown structure-property model without the need for an *ansatz* of its analytical form.

5.2.1 Inference Accuracy

To quantify the accuracy of the inference results, I calculated the average integrated relative error between the inferred model and the true model. Because the GB diffusivity structure-property models span orders of magnitude, care must be taken when computing differences. For example, a deviation of one might be very small in a region where a function is on the order of 10^2, but could be very large in another region where that function is on the order of 10^{-2}. To address this issue, I calculate the error on a logarithmic scale:

$$\text{average integrated relative error} = \frac{\int \left| \frac{\log\left(\hat{\mathscr{D}}(\mathbf{\Omega}, \mathbf{D})\right) - \log\left(\mathscr{D}(\mathbf{\Omega})\right)}{\log\left(\mathscr{D}(\mathbf{\Omega})\right)} \right| \mathrm{d}\mathbf{\Omega}}{\int \mathrm{d}\mathbf{\Omega}} \tag{5.4}$$

where $\mathbf{\Omega} = \{\omega\}$ in the 1DOF case, $\mathbf{\Omega} = \{\omega, \theta, \phi\}$ in the 3DOF case, and $\mathbf{\Omega} = \{\omega, \theta, \phi\, \alpha, \beta\}$ in the 5DOF case; the domain as well as the differential volume element are chosen appropriately. The average integrated relative error describes the average error (across the entire domain) that would be expected from a prediction made using the inference result. The integration of Equation (5.4) for 1DOF cases is carried out numerically using the trapezoidal rule. For the 3DOF and 5DOF cases Monte-Carlo integration is employed [85].

The results of the average integrated relative error for each of the models are presented in Table 5.1. With a high frequency of observations in every bin, the value of $\sigma\left(\{\mathbf{D}, \mathbf{M}\}\right)$ for the most probable model was large and the error was quite low, even for the 3DOF case, which has a more coarse discretization than the 1DOF case. The results also show that in the 5DOF case the error is not unreasonably high, however, it is admittedly higher. There are two possible explanations for this phenomenon that I want to discuss. One, the GB character distribution (GBCD) might affect

Table 5.1: Average integrated relative error of the inferred models.

Model	Average Integrated Relative Error (%)
1DOF BRK	0.9937
1DOF Exponential (Equation (5.2))	9.6063
3DOF	0.9271
5DOF	2.5003

the accuracy of the inference and will be discussed further in Section 5.2.2. Two, the discretization resolution and number of microstructures used for each inference process also influence the accuracy of the inference as will be discussed in Section 5.2.3.

5.2.2 Influence of GBCD

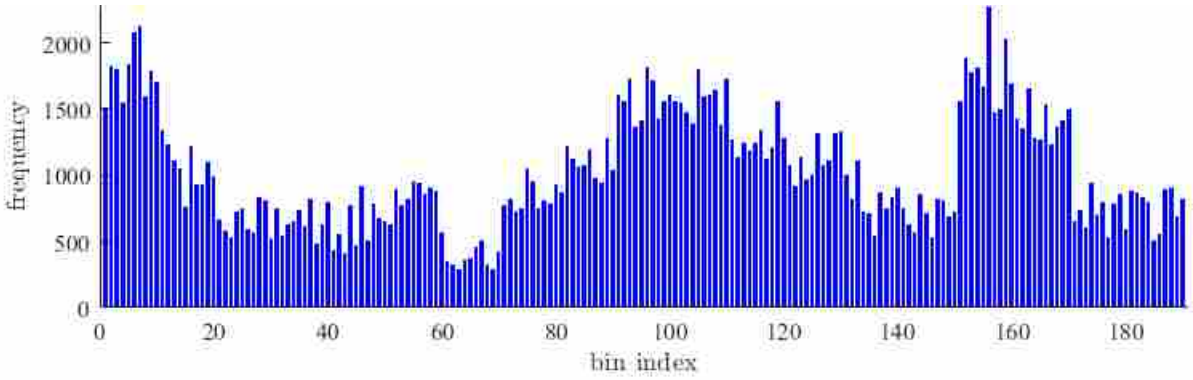

Figure 5.5: The GBCD for the 5DOF case across all of the employed polycrystals to obtain inference result displayed in Figure 5.3.

As has been mentioned, the average integrated relative error is low (see Table 5.1) when the frequency of observations in every bin is high. However, in other 1DOF and 3DOF tests, I observed that if bins with little to no data exist, then the optimal value of $\sigma(\{\mathbf{D},\mathbf{M}\})$ was smaller and the error of the inferred model was larger. To inspect this factor in 5DOF case, I plot the frequency of GB segments in each bin (see Figure 5.5). From Figure 5.5, we can see that the GB distribution is highly not uniform with little data in some of the bins. However, there is no evidence that the accuracy can be increased by using more uniform GBCD and further inspection about this influence need to be performed in the future.

5.2.3 Influence of Discretization Resolution and Number of Microstructures

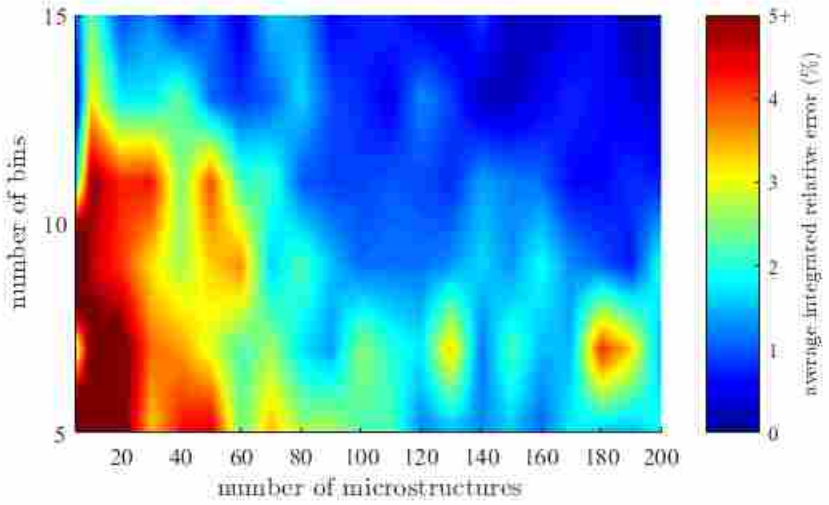

Figure 5.6: Comparison of the average integrated relative error of the inference using different numbers of bins and microstructures. In this comparison, we used the 1DOF BRK model. The color-scale is clipped at 5% so that the region of interest, which has low error, is visible; however, higher errors were observed when the number of bins was extremely small.

To investigate the influence of discretization resolution, bin frequency, and their interaction, I performed localization for the 1DOF BRK model using different numbers of bins and microstructures. As can be seen in Figure 5.6, the finer the resolution of the discretization (i.e. the more bins that were employed) the lower the error in the inference. However, there also appears to be a number of bins above which the reduction of the relative error is not significant (approximately 10 for large numbers of microstructures). Consistent with intuition, the use of more microstructures also leads to improved inference, likely due to a higher frequency of observations in every bin (and avoiding empty bins). However, I again observe a saturation point above a certain number of microstructures (100 in the present case, which is the reason that 100 microstructures were used in the results of Section 5.1), where there is little to no added benefit. Although not overly burdensome for a computational endeavor, 100 microstructures could constitute a significant experimental effort. It is, therefore, worth noting that even for small numbers of microstructures accurate inference is possible. For example, with 20 microstructures and 15 bins, the average integrated relative error for the inferred 1DOF BRK model was about 1.08%.

The investigation to the 1DOF BRK model above confirms the possibility to obtain a better inference in 5DOF case using a finer discretization and/or more microstructures. However, using finer resolution might introduce a couple problems: $(\mathbf{1})$ using finer resolution (more number of bins) is also increase the possibility of bin with little to no data to existing which can lower the accuracy of the inference; $(\mathbf{2})$ using finer resolution makes $\sigma\left(\{\mathbf{D},\mathbf{M}\}\right)$ exist in higher dimensional space that also increases the computational cost.

The other option to increase the accuracy of the inference is by using more microstructures. Using more microstructures, however, makes the computational cost more expensive than my currently available resources. Thus, an alternative route is needed. Here, for the 5DOF case, I parallelized the inference process by dividing the 2000 samples into pools of 100 polycrystals. The inference process was then performed for each pool of polycrystals before combining the result using the KDE method [66] (see [67] for a MATLAB implementation). The KDE method used to obtain the diffusivity value in each bin which has the highest density; I call this approach as the KDE approach.

To make the KDE approach clearer, let us consider a 1DOF example in which the domain of the structure-property model is discretized into five bins (see Figure 5.7. Doing inference process multiple times with different set of polycrystals, each inference process gives an approximate constitutive model displayed as the colored lines in Figure 5.7 (lines with the same color belongs to the same model). Using the KDE method, I can then estimate the marginal density of the results in each bin (the dashed black lines in Figure 5.7). The diffusivity values in each bin which has the highest density are then picked (the black lines in Figure 5.7). This collection of the diffusivity values in each bin become an inferred constitutive model which can be compared to the "actual" model (the dashed gray line in Figure 5.7).

Employing the KDE approach explained above, I performed the inference for the same problem as presented in Section 5.1.3 and obtained the result displayed in Figure 5.8. The result in Figure 5.8 shows that the KDE approach of GB property localization gives a satisfactory approximation to the constitutive model. The average integrated relative error for this result, calculated using Equation (5.4), is about 0.25%. With the encouraging result in the 5DOF case without noise, I tested the approach for the 5DOF case where I introduced $\varepsilon \sim N\left[0, \left(0.5\% \left(\bar{D}^{\mathrm{SGT}}\right)\right)^2\right]$ noise to Equation (4.1) (see Figure 5.9 for the inference result). The results of this case also show a satis-

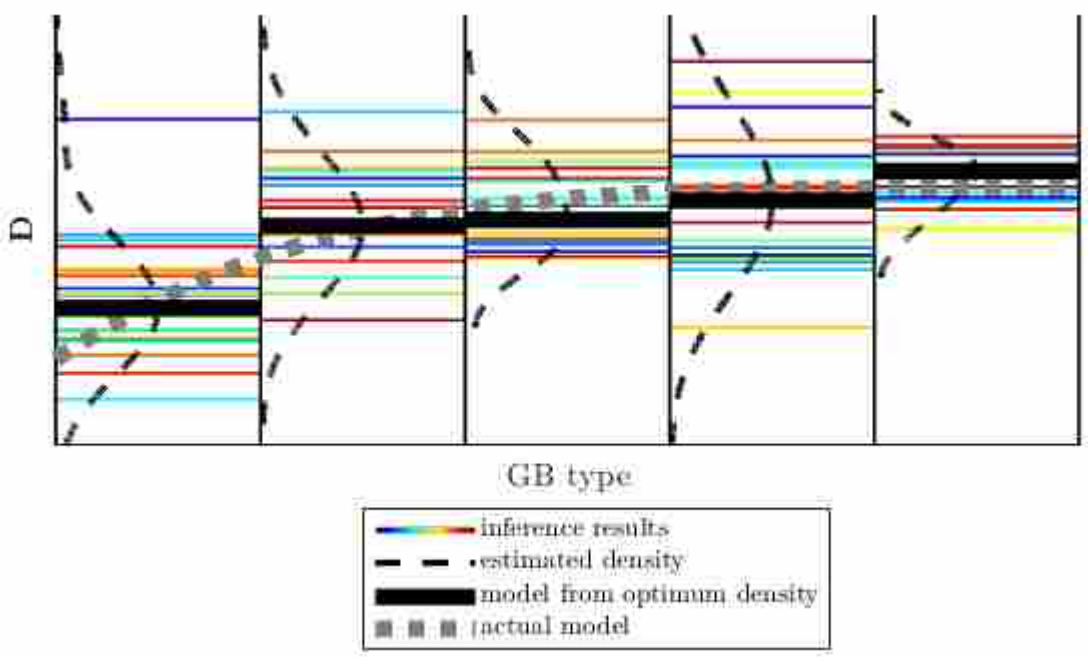

Figure 5.7: Illustration of the KDE approach. The figure shows the 1DOF case where the domain is discretized into five bins. The colored lines are the approximate constitutive models obtained from the inference processes with different set of polycrystals (each model is indicated by the same line's color). The dashed black line at each bin is the estimated density distribution. The black lines are the model from the optimum density. The dashed gray line is the actual model.

factory approximation to the constitutive model with the average integrated relative error close to 0.69%. However, since manufacturing 2000 polycrystals can be burdensome and the application of the KDE approach to the problem with more realistic observation noise is still unknown, a different approach or a further inspection of the use of KDE approach is needed in the future study.

5.2.4 Limitations of the Piece-wise Constant Function

Utilizing a piece-wise constant function for $\widehat{\mathscr{D}}$ may introduce accuracy problems in the region of the model where the slope is large. For example, in the 1DOF cases, for the bin where $\omega = [0^\circ, 4.5^\circ]$, $\widehat{\mathscr{D}}$ predicts a constant value of diffusivity while the actual value of the diffusivity spans orders of magnitude. To evaluate the impact of using a piece-wise constant function, I calculated the average integrated relative error in each bin for both 1DOF models, with the bin limits serving as the integration limits in Equation (5.4). To highlight which region of the models have small vs. large gradient, I plotted both models on a linear scale and calculated the approximate

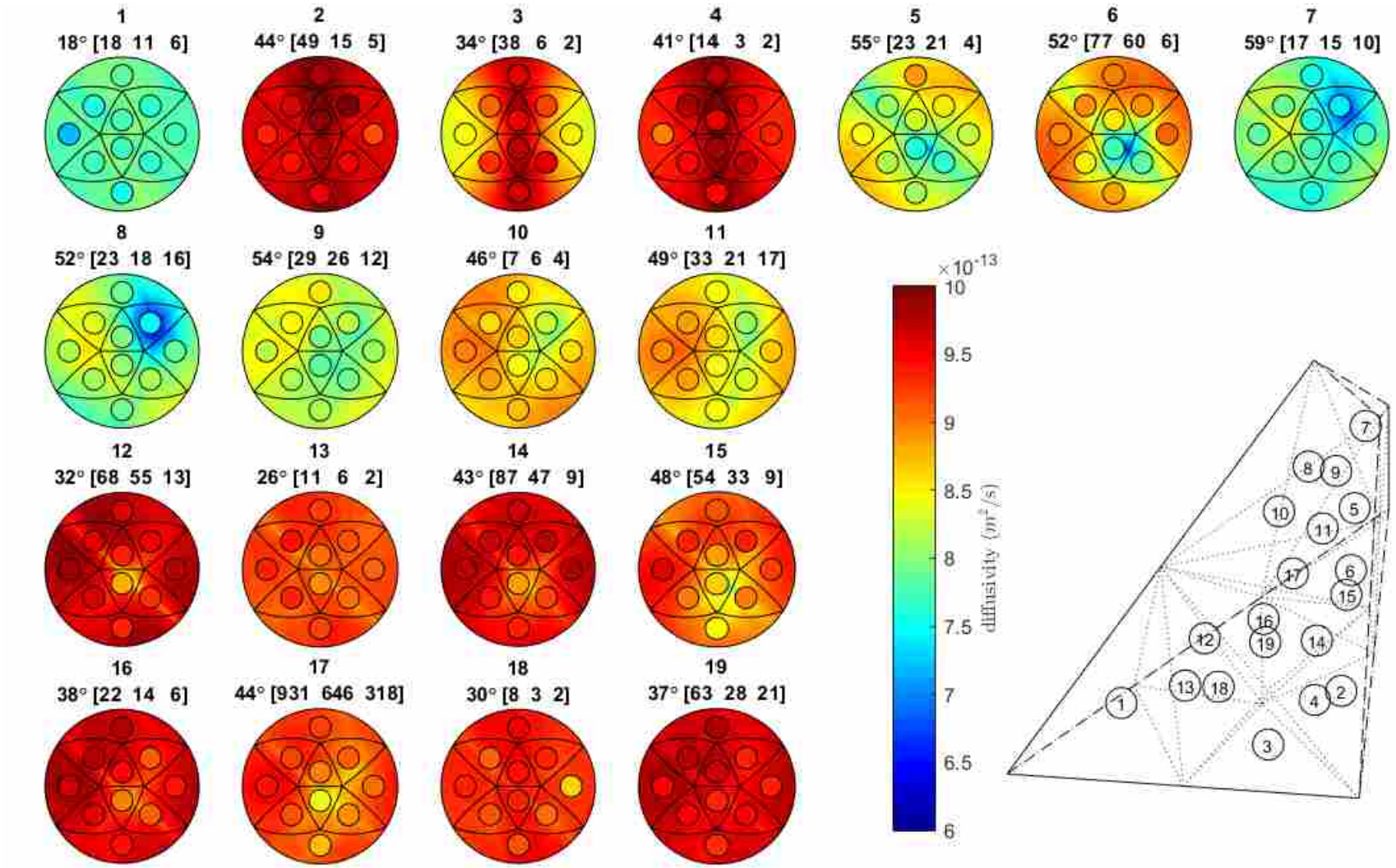

Figure 5.8: GB property localization result utilizing the KDE approach, applied to the problem presented in Section 5.1.3. Each big circle is the stereographic projection of the hemisphere (GB plane FZ) corresponding to the center of the bin in the disorientation FZ. The color of the hemisphere represents the true diffusivity value and the small circular markers indicate the inferred diffusivity value in each bin using the same color scale.

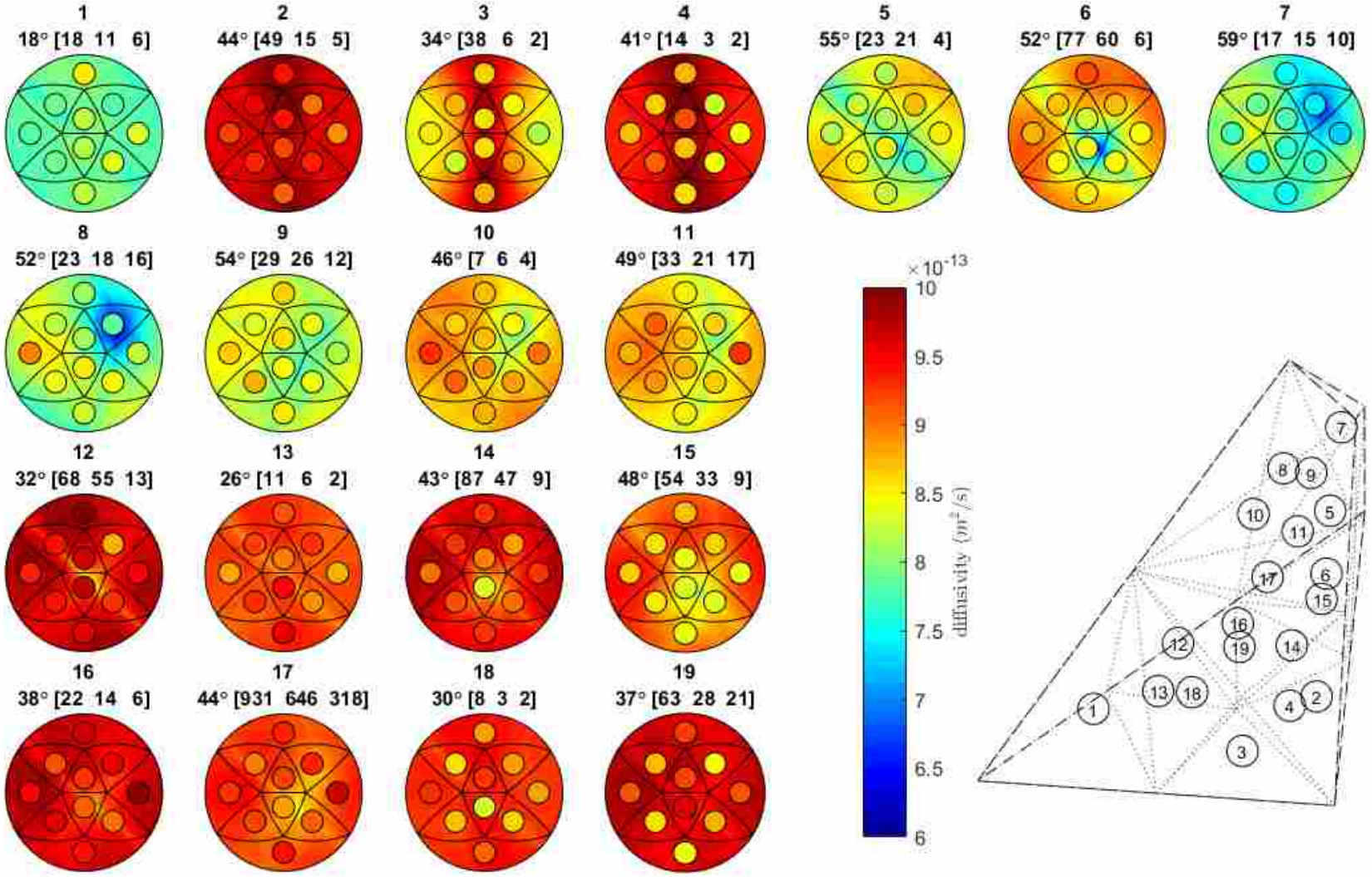

Figure 5.9: GB property localization result utilized the KDE approach, applied to the problem where $\varepsilon \sim N\left[0, \left(0.5\% \left(\bar{D}^{\mathrm{SGT}}\right)\right)^2\right]$ noise to Equation (4.1) is introduced. Each big circle is the stereographic projection of the hemisphere (GB plane FZ) corresponding to the center of the bin in the disorientation FZ. The color of the hemisphere represents the true diffusivity value and the small circular markers indicate the inferred diffusivity value in each bin using the same color scale.

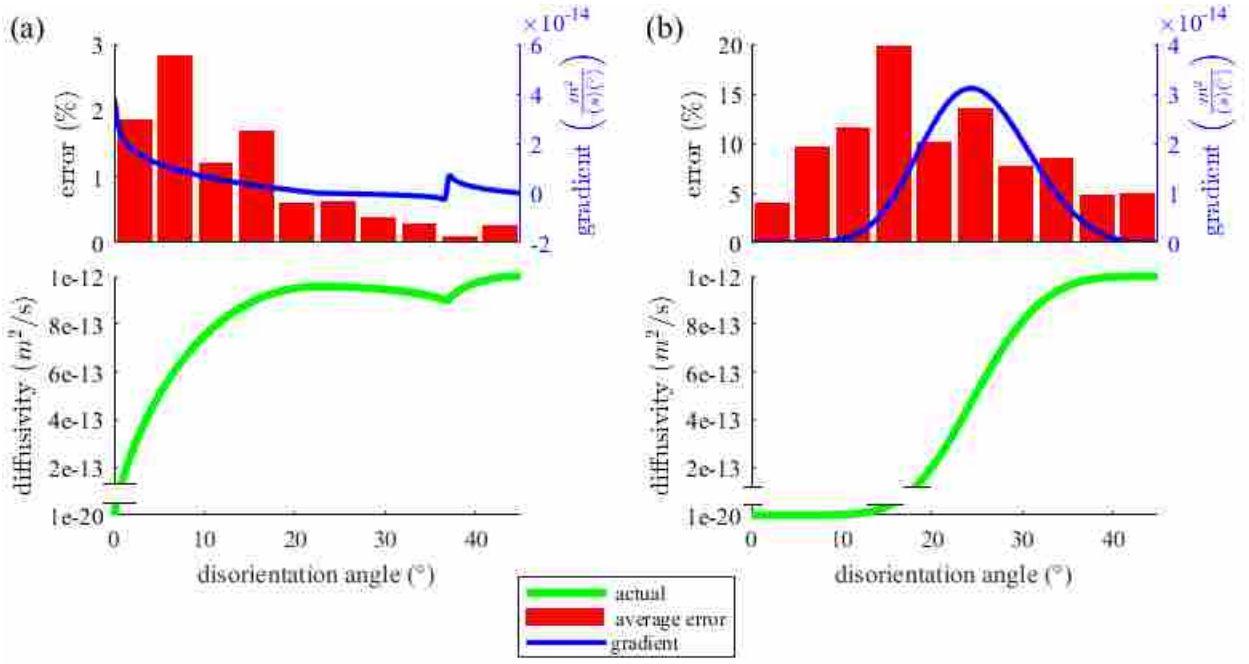

Figure 5.10: The average integrated relative error in each bin for (a) the 1DOF BRK model case and (b) 1DOF exponential function of Equation (5.2). In contrast to Figure 5.1, both models are plotted on a linear scale to clearly highlight which regions have small vs. large gradients with the blue lines indicate the approximate gradient of the functions.

gradient numerically (shown as the blue lines in Figure 5.10). Figure 5.10 shows that the percent error of the inferred model is relatively larger in regions where the gradient is larger, as expected. Similarly, in Table 5.1, the higher error in the inference of the 1DOF exponential model (Equation (5.2)) also reflects this limitation of the piece-wise constant version of $\widehat{\mathscr{D}}$, as Equation (5.2) exhibits a broader region (about 12° to 35°) with relatively high gradient compared to the BRK model (about 0° to 10°). Consequently, I suggest that a piece-wise linear (or other low-order polynomial) form of $\widehat{\mathscr{D}}$ may increase the fidelity of the inference while remaining largely agnostic to the underlying model to be inferred (which was the original purpose for employing the piece-wise linear form).

5.2.5 Singularity

As mentioned previously, the models that I selected/constructed were intended to help evaluate how well certain qualitative features that we might expect in a real GB diffusivity structure-

property model could be captured by the property localization method. To verify how well the localization approach captures the singularity in the 1DOF BRK model, I calculated the average integrated relative error for the bin that contained the singularity. Figure 5.1 and Figure 5.10 show that even though the bin containing the cusp had nearly the fewest observations, it had the lowest error (0.0891%) and one of the lowest levels of uncertainty, even in the presence of observation noise. Rather than being challenging to infer, my observations suggest that the localization approach may be particularly well-suited to inferring structure-property models containing cusps. This is encouraging news since real GB structure-property models are expected to exhibit these features.

CHAPTER 6. CONCLUSION

In this work, I developed a Bayesian approach to GB property localization to infer a constitutive (structure-property) model for GB properties from measurements of the effective properties of polycrystals without *a priori* knowledge of the form of the model, in the presence of observation noise (i.e. measurement uncertainty). The inference is done by approximating the constitutive model in a form of piece-wise constant function and then calculate the probability of the proposed model to be consistent with the observed effective properties using a PDF derived in this thesis. The derivation of the PDF that is specific for GB diffusivity was presented from the general form of the inverse problem theory by considering some idealized assumptions. However, because the derivation presented was quite general by using the Bayesian approach, the method should be modifiable to meet different conditions and assumptions including, *e.g.*, the application for other properties of interest. The inferred model is the proposed model that has the highest probability to be consistent with the observed effective diffusivity. Here, I also presented an adjustment to the optimization process to compensate the nature of the PDF which can be challenging to converge.

The nature of the method which utilize the Bayesian probability approach makes the uncertainty quantification possible to perform. I demonstrated how uncertainty quantification for the inferred structure-property models is easily performed within the idealized case framework by utilizing the Metropolis-Hastings algorithm and KDE method.

I tested the method for 1DOF, 3DOF, and 5DOF cases, calculated the average integrated relative error of the inference (see Table 5.1), and demonstrated how uncertainty quantification for the inference result may be included in the method. The validation in 1DOF and 3DOF cases were performed by considering a pool of 1771 two-dimensional simulated polycrystals which generated using a method that encourage the diversity of GBN structure. Using randomly picked 100 polycrystals from this pool and considering the BRK function as the test model, I observed satisfactory inference accuracy, even using a relatively coarse discretization and in the presence of observation

noise, with average integrated relative error less than 1%. The validation in 1DOF BRK case also indicated that the inference method may be well-suited to capture the singularity possessed by the test model with the bin containing the cusp exhibiting among the lowest average integrated relative error (0.0891%) and uncertainty. However, the average integrated relative error of the inferred model with the exponential function (Equation (5.2)) as the test model was relatively higher. From the inspection of the correlation between the gradient of the model and the error, presented in this thesis, I conclude that the relatively higher error in 1DOF exponential case could be caused by the limitation of the piece-wise constant function as the form for $\widehat{\mathscr{D}}$.

The validation in 5DOF case was performed by considering a pool of 2000 three-dimensional simulated polycyrstals generated using Neper software version 3.0.2 [75–78]. Using randomly picked 100 polycyrstals from this pool and considering the BRK function as the test model, I observed that the inference result still has noticeable error, even when no observation noise was introduced. The lower accuracy in this case could be caused by the GBCD which was not uniform enough compare to the 1DOF and 3DOF cases. However, further inspection about this influence need to be performed in the future. Another possible explanation to the lower accuracy in this case is the influence of the discretization resolution and the number of microstrcutures used in the inference process. However, because the computational cost become prohibitive when more microstructures are used to increase the accuracy of the inference, I proposed a method to parallelize the localization inference into pools and use KDE method to combine the inference results and estimate the model, I called as the KDE approach. Using the KDE approach for 5DOF case with total of 2000 polycrystals, I observed satisfactory inference accuracy with average integrated relative error close to 0.3%. However, since manufacturing 2000 polycrystals can be burdensome and the application of the KDE approach to the problem with more realistic observation noise is still unknown, a different approach or a further inspection of the use of KDE approach is needed in the future study.

In this study a GB localization method was developed and validated by considering hypothetical constitutive models for GB diffusivity. The validation result implies that the method might be a more efficient strategy for inferring GB structure-property models. Diffusivity is an obvious application, but the property localization inference method presented here should also be applicable to other properties of interest for which a suitable homogenization relation is available. However,

the refinement of the 5DOF case and consideration of the application to experimental/simulation data to infer actual unknown structure-property models are still needed. Further improvements to the approach may also include refinement of the form employed for $\widehat{\mathscr{D}}$ (*e.g.* piece-wise linear).

REFERENCES

[1] Wikipedia, Grain Boundary (2007).
URL https://en.wikipedia.org/wiki/Grain_boundary

[2] University of Cambridge, Dislocation in 2D (2004).
URL http://www.doitpoms.ac.uk/tlplib/dislocations/dislocations_in_2D.php

[3] P. Lejcek, Grain Boundaries : Description , Structure, and Thermodynamics, in: P. Lejcek (Ed.), Grain boundary Segregation in Metals, xiii Edition, Springer, 2010, Ch. 2, pp. 5–24. doi:10.1007/978-3-642-12505-8.

[4] J. K. Mason, C. A. Schuh, Correlated grain-boundary distributions in two-dimensional networks., Acta crystallographica. Section A, Foundations of crystallography 63 (Pt 4) (2007) 315–28. doi:10.1107/S0108767307021782.
URL http://scripts.iucr.org/cgi-bin/paper?pz5039

[5] W. T. Read, W. Shockley, Dislocation Models of Crystal Grain Boundaries, Physical Review.

[6] D. L. Olmsted, S. M. Foiles, E. A. Holm, Survey of computed grain boundary properties in face-centered cubic metals: I. Grain boundary energy, Acta Materialia 57 (13) (2009) 3694–3703. doi:10.1016/j.actamat.2009.04.007.
URL http://dx.doi.org/10.1016/j.actamat.2009.04.007

[7] E. M. Lehockey, On improving the corrosion and growth resistance of positive Pb-acid battery grids by grain boundary engineering, Power Sources (1999) 79–83.

[8] E. M. Lehockey, G. Palumbo, On the creep behaviour of grain boundary engineered nickel , Materials Science and Engineering A 237 (1997) 168–172.

[9] E. M. Lehockey, G. Palumbo, P. Lin, Improving the Weldability and Service Performance of Nickel- and Iron-Based Superalloys by Grain Boundary Engineering, Metallurgical and Materials Transactions A 29 (December) (1998) 3069–3079.

[10] D. P. Norton, A. Goyal, J. D. Budai, D. K. Christen, D. M. Kroeger, E. D. Specht, Q. He, B. Saffian, M. Paranthaman, C. E. Klabunde, D. F. Lee, B. C. Sales, F. A. List, Epitaxial YBa2Cu307 on Biaxially Textured Nickel (001): An Approach to Superconducting Tapes with High Critical Current Density Published by : American Association for the Advancement of Science, Science 274 (001) (1996) 755–757.

[11] Y. Chen, C. a. Schuh, Diffusion on grain boundary networks: Percolation theory and effective medium approximations, Acta Materialia 54 (18) (2006) 4709–4720. doi:10.1016/j.actamat.2006.06.011.

[12] A. Oudriss, J. Creus, J. Bouhattate, E. Conforto, C. Berziou, C. Savall, X. Feaugas, Grain size and grain-boundary effects on diffusion and trapping of hydrogen in pure nickel, Acta Materialia 60 (19) (2012) 6814–6828. doi:10.1016/j.actamat.2012.09.004.
URL http://dx.doi.org/10.1016/j.actamat.2012.09.004

[13] V. Randle, V. Randle, Grain boundary engineering : an overview after 25 years Grain boundary engineering : an overview after 25 years, Materials Science and Technology 0836 (August). doi:10.1179/026708309X12601952777747.

[14] L. C. Lim, T. Watanabe, FRACTURE TOUGHNESS AND BRITTLE-DUCTILE TRANSITION CONTROLLED BY GRAIN BOUNDARY CHARACTER DISTRIBUTION (GBCD) IN POLYCRYSTALS, Acta metall, mater. 38 (12) (1990) 2507–2516.

[15] S. M. Schlegel, S. Hopkins, M. Frary, Effect of grain boundary engineering on microstructural stability during annealing, Scripta Materialia 61 (1) (2009) 88–91. doi:10.1016/j.scriptamat.2009.03.013.
URL http://dx.doi.org/10.1016/j.scriptamat.2009.03.013

[16] D. L. Engelberg, R. C. Newman, T. J. Marrow, Effect of thermomechanical process history on grain boundary control in an austenitic stainless steel, Acta Materialia 59 (2008) 554–557. doi:10.1016/j.scriptamat.2008.05.012.

[17] G. Palumbo, E. M. Lehockey, P. Lin, Applications for Grain Boundary Engineered Materials, The Journal of The Minerals, Metals & Materials Society (TMS) 600 (February) (1998) 3–6.

[18] L. Tan, K. Sridharan, T. R. Allen, Effect of thermomechanical processing on grain boundary character distribution of a Ni-based superalloy, Journal of Nuclear Materials 371 (2007) 171–175. doi:10.1016/j.jnucmat.2007.05.002.

[19] I. Kaur, Y. Mishin, W. Gust, Fundamentals of Grain and Interphase Boundary Diffusion, 3rd Edition, Willey, 1995.

[20] R. C. Hugo, R. G. Hoagland, Kinetics of gallium penetration into aluminum grain boundaries - in situ TEM observations and atomistic models, Acta Materialia 48 (8) (2000) 1949–1957. doi:10.1016/S1359-6454(99)00463-2.

[21] D. L. Olmsted, E. A. Holm, S. M. Foiles, Survey of computed grain boundary properties in face-centered cubic metals-II: Grain boundary mobility, Acta Materialia 57 (13) (2009) 3704–3713. doi:10.1016/j.actamat.2009.04.015.
URL http://dx.doi.org/10.1016/j.actamat.2009.04.015

[22] A. D. Rollett, C. C. Yang, W. W. Mullins, B. L. Adams, C. T. Wu, D. Kinderlehrer, S. Ta'asan, F. Manolache, C. Liu, I. Livshits, D. Mason, A. Talukder, S. Ozdemir, D. Casasent, A. Morawiec, D. Saylor, G. S. Rohrer, M. Demirel, B. El-Dasher, W. Yang, Grain boundary property determination through measurement of triple junction geometry and crystallography, Recrystallization and Grain Growth, Vols 1 and 2 (2001) 165–175.
URL <GotoISI>://WOS:000175295500015

[23] V. V. Bulatov, B. W. Reed, M. Kumar, Grain boundary energy function for fcc metals, Acta Materialia 65 (2014) 161–175. doi:10.1016/j.actamat.2013.10.057.
URL http://dx.doi.org/10.1016/j.actamat.2013.10.057

[24] M. Binci, D. Fullwood, S. R. Kalidindi, A new spectral framework for establishing localization relationships for elastic behavior of composites and their calibration to finite-element models, Acta Materialia 56 (10) (2008) 2272–2282. doi:10.1016/j.actamat.2008.01.017.

[25] T. Fast, S. R. Kalidindi, Formulation and calibration of higher-order elastic localization relationships using the MKS approach, Acta Materialia 59 (11) (2011) 4595–4605. doi:10.1016/j.actamat.2011.04.005.
URL http://dx.doi.org/10.1016/j.actamat.2011.04.005

[26] D. T. Fullwood, S. R. Kalidindi, B. L. Adams, S. Ahmadi, A discrete fourier transform framework for localization relations, Computers, Materials and Continua 9 (1) (2009) 25–39. doi:10.3970/cmc.2009.009.025.

[27] S. R. Kalidindi, G. Landi, D. T. Fullwood, Spectral representation of higher-order localization relationships for elastic behavior of polycrystalline cubic materials, Acta Materialia 56 (15) (2008) 3843–3853. doi:10.1016/j.actamat.2008.01.058.

[28] G. Landi, S. R. Kalidindi, Thermo-elastic localization relationships for multi-phase composites, Computers, Materials and Continua 16 (3) (2010) 273–293. doi:10.3970/cmc.2010.016.273.

[29] Y. C. Yabansu, D. K. Patel, S. R. Kalidindi, Calibrated localization relationships for elastic response of polycrystalline aggregates, Acta Materialia 81 (2014) 151–160. doi:10.1016/j.actamat.2014.08.022.
URL http://dx.doi.org/10.1016/j.actamat.2014.08.022

[30] Y. C. Yabansu, S. R. Kalidindi, Representation and calibration of elastic localization kernels for a broad class of cubic polycrystals, Acta Materialia 94 (2015) 26–35. doi:10.1016/j.actamat.2015.04.049.
URL http://dx.doi.org/10.1016/j.actamat.2015.04.049

[31] D. Y. Li, J. A. Szpunar, Determination of single crystals' elastic constants from the measurement of ultrasonic velocity in the polycrystalline material, Acta Metallurgica Et Materialia 40 (12) (1992) 3277–3283. doi:10.1016/0956-7151(92)90041-C.

[32] M. Hayakawa, S. Imai, M. Oka, Determination of single-crystal elastic constants from a cubic polycrystalline aggregate, Journal of Applied Crystallography 18 (1985) 513–518. doi:10.1107/S0021889885010809.

[33] D. K. Patel, H. F. Al-Harbi, S. R. Kalidindi, Extracting single-crystal elastic constants from polycrystalline samples using spherical nanoindentation and orientation measurements, Acta Materialia 79 (2014) 108–116. doi:10.1016/j.actamat.2014.07.021.

[34] O. K. Johnson, L. Li, M. J. Demkowicz, C. A. Schuh, Inferring grain boundary structureproperty relations from effective property measurements, Journal of Materials Science 50 (21)

(2015) 6907–6919. doi:10.1007/s10853-015-9241-4.
URL http://link.springer.com/10.1007/s10853-015-9241-4

[35] W. D. Callister, D. G. Rethwisch, Materials Science and Engineering: an Introduction, 8th Edition, Wiley, 2009.

[36] A. P. Sutton, R. W. Balluffi, Interfaces in crystalline materials, Clarendon Press, 1995.

[37] D. L. Olmsted, A new class of metrics for the macroscopic crystallographic space of grain boundaries, Acta Materialia 57 (9) (2009) 2793–2799. doi:10.1016/j.actamat.2009.02.030.

[38] C. C. Mei, J.-L. Auriault, C.-O. Ng, Some Applications of the Homogenization Theory, Advances in Applied Mechanics 32 (1996) 277 – 348. doi:10.1207/s15327752jpa8502.

[39] G. Allaire, INTRODUCTION TO HOMOGENIZATION THEORY.
URL http://www.cmap.polytechnique.fr/~allaire/homog/lect1.pdf

[40] D. D. Cioranescu, P. Donato, An Introduction to Homogenization, Oxford University Press, 1999.

[41] E. Sanchez-Palencia, Homogenization in Mechanics, a Survey of Solved and Open Problems, Rend. Sem. Mat. Univ. Politec. ... 44 (1986) 1–46.
URL http://www.seminariomatematico.unito.it/rendiconti/cartaceo/44-1/1.pdf

[42] L. Tartar, The General Theory of Homogenization: A Personalized Introduction (Google eBook), Springer, 2009. doi:10.1007/978-3-642-05195-1.
URL http://books.google.com/books?id=P51k82nS_d0C&pgis=1

[43] G. A. Pavliotis, Homogenization theory for advection-diffusion equations with mean flow, Ph.D. thesis, Rensselaer Polytechnic Institute (2002).
URL http://gateway.proquest.com/openurl?url_ver=Z39.88-2004&rft_val_fmt=info:ofi/fmt:kev:mtx:dissertation&res_dat=xri:pqdiss&rft_dat=xri:pqdiss:3057679

[44] O. K. Johnson, E. R. Homer, D. T. Fullwood, Using the Effective Diffusivity of Polycrystals to Infer a Complete 5D Structure-Property Model for Hydrogen Diffusivity in Iron Grain Boundaries (2016).

[45] E. Hart, Letters to the Editor On the Role of Dislocations in Bulk Diffusion, Acta Metallurgica 5 (1954) (1957) 597. doi:10.1016/0001-6160(57)90127-X.

[46] S. Kirkpatrick, Percolation and Conduction, Reviews of Modern Physics 45 (4) (1973) 574–588. doi:10.1103/RevModPhys.45.574.
URL http://link.aps.org/doi/10.1103/RevModPhys.45.574

[47] T. C. Choy, Effective Medium Theory: Principles and Applications, Clarendon Press, 1999.

[48] S. R. Broadbent, J. M. Hammersley, Percolation Processes I. Crystals and Mazes, Mathematical Proceedings of the Cambridge Philosophical Societydoi:10.1017/S0305004100032692.

[49] B. Bollobás, O. Riordan, Percolation, Cambridge University Press, 2006.

[50] H. Kesten, Percolation Theory for Mathematicians, Birkhauser, 1982.

[51] D. Stauffer, Introduction to Percolation Theory, Taylor & Francis, 1985.

[52] J. M. Hammersley, Percolation Processes: Lower Bound for The Critical Probability, The Annals of Mathematical Statistics.
URL http://www.jstor.org/stable/2237242

[53] J. M. Hammersley, Percolation Processes II. The Connective Constant, Mathematical Proceedings of the Cambridge Philosophical Societydoi:10.1017/S0305004100032692.

[54] D. S. McLachlan, An equation for the conductivity of binary mixtures with anisotropic grain structures, Physica C: Solid state.
URL http://iopscience.iop.org/0022-3719/20/7/004/pdf/0022-3719_20_7_004.pdf

[55] D. S. McLachlan, Measurement and analysis of a model dual-conductivity medium using a generalised effective-medium theory, Journal of Physics C: Solid State Physics 21 (8) (1988) 1521–1532. doi:10.1088/0022-3719/21/8/025.
URL http://stacks.iop.org/0022-3719/21/i=8/a=025

[56] O. K. Johnson, J. M. Lund, T. R. Critchfield, Spectral graph theory for characterization and homogenization of grain boundary networks, Acta Materialia 146 (2018) 42–54. doi:10.1016/j.actamat.2017.11.054.

[57] A. Tarantola, Inverse Problem Theory and Methods for Model Parameter Estimation, Society for Industrial and Applied Mathematics, Philadelphia, 2005.

[58] A. Tarantola, B. Valette, Inverse Problems = Quest for Information, Journal of Geophysics 50 (3) (1982) 159–170. doi:10.1038/nrn1011.
URL http://www.ipgp.fr/~tarantola/Files/Professional/Papers_PDF/IP_QI_latex.pdf

[59] K. Mosegaard, A. Tarantola, Probabilistic Approach to Inverse Problems, in: International Handbook of Earthquake & Engineering Seismology (Part A), Academic Press, 2002, pp. 237–265. doi:10.1016/S0074-6142(02)80219-4.

[60] R. Aggarwal, M. J. Demkowicz, Y. M. Marzouk, Bayesian inference of substrate properties from film behavior, Modelling and Simulation in Materials Science and Engineering 23 (1) (2015) 0–15. doi:10.1088/0965-0393/23/1/015009.

[61] R. Aggarwal, M. J. Demkowicz, Y. M. Marzouk, Information-Driven Experimental Design in Materials Science, in: Information Science for Materials Discovery and Design, Vol. 225, Springer, 2016, pp. 13 – 44. doi:10.1007/978-3-319-23871-5.

[62] A. N. Kolmogorov, FOUNDATIONS OF THE THEORY OF PROBABILITY, second eng Edition, CHELSEA PUBLISHING COMPANY, New York, New York, USA, 1956.

[63] The MathWorks, MATLAB 2017a (2017).
URL https://www.mathworks.com/products/matlab.html

[64] J. A. Nelder, R. Mead, A Simplex Method for Function Minimization, The Computer Journal 7 (4) (1965) 308–313. doi:10.1093/comjnl/7.4.308.
URL https://academic.oup.com/comjnl/article-lookup/doi/10.1093/comjnl/7.4.308

[65] J. D'Erico, fminsearchbnd v.1.4, Bound constrained optimization using fminsearch (2012).
URL https://www.mathworks.com/matlabcentral/fileexchange/8277-fminsearchbnd--fminsearchcon

[66] Z. I. Botev, J. F. Grotowski, D. P. Kroese, Kernel density estimation via diffusion, Annals of Statistics 38 (5) (2010) 2916–2957. doi:10.1214/10-AOS799.

[67] Z. I. Botev, Kernel Density Estimator V.1.5 (2015).
URL https://www.mathworks.com/matlabcentral/fileexchange/14034-kernel-density-estimator?s_tid=prof_contriblnk

[68] E. A. Lazar, R. D. Macpherson, D. J. Srolovitz, A more accurate two-dimensional grain growth algorithm, Acta Materialia 58 (2009) 364–372. doi:10.1016/j.actamat.2009.09.008.
URL http://ac.els-cdn.com/S135964540900603X/1-s2.0-S135964540900603X-main.pdf?_tid=3270f958-8c31-11e7-9c9a-00000aacb361&acdnat=1503953038_1e46c1df84489139c05785710d1ce186

[69] M. Frary, C. A. Schuh, Grain boundary networks: Scaling laws, preferred cluster structure, and their implications for grain boundary engineering, Acta Materialia 53 (16) (2005) 4323–4335. doi:10.1016/j.actamat.2005.05.030.

[70] E. Science, G. Britain, M. S. Laboratories, I. Engineering, M. S. Problems, R. Academy, Computer Simulation Study of Grain Boundary and Triple Junction Distributions in, Acta metall, mater. 43 (6) (1995) 2317–2324.

[71] O. K. Johnson, C. A. Schuh, The uncorrelated triple junction distribution function: Towards grain boundary network design, Acta Materialia 61 (8) (2013) 2863–2873. doi:10.1016/j.actamat.2013.01.025.

[72] P. Fortier, Triple Junction and Grain Boundary Character Distributions in Metallic Materials, Acta mater. 45 (8) (1997) 4–9.

[73] Y. S. Yi, J. S. Kim, Characterization methods of grain boundary and triple junction distributions, Scripta Materialia 50 (6) (2004) 855–859. doi:10.1016/j.scriptamat.2003.12.010.

[74] P. Davies, V. Randle, G. Watkins, H. Davies, Triple junction distribution profiles as assessed by electron backscatter diffraction, Journal of Materials Science 37 (19) (2002) 4203–4209. doi:10.1023/A:1020052306493.

[75] R. Quey, P. R. Dawson, F. Barbe, Large-scale 3D random polycrystals for the finite element method: Generation, meshing and remeshing, Computer Methods in Applied Mechanics and Engineering 200 (17-20) (2011) 1729–1745. doi:10.1016/j.cma.2011.01.002.
URL http://dx.doi.org/10.1016/j.cma.2011.01.002

[76] R. Quey, Neper Reference Manual The documentation for Neper 3.0.2 A software package for polycrystal generation and meshing (2017).
URL http://neper.sourceforge.net/

[77] R. Quey, L. Renversade, Optimal polyhedral description of 3D polycrystals: Method and application to statistical and synchrotron X-ray diffraction data, Computer Methods in Applied Mechanics and Engineering 330 (2018) 308–333. doi:10.1016/j.cma.2017.10.029.

[78] R. Quey, Polycrystal Generation and Meshing — Neper 3.0.2.
URL http://neper.sourceforge.net/

[79] S. Ifergane, E. Sabatani, B. Carmeli, Z. Barkay, V. Ezersky, O. Beeri, N. Eliaz, Hydrogen diffusivity measurement and microstructural characterization of Custom 465 stainless steel, Electrochimica Acta 178 (January) (2015) 494–503. doi:10.1016/j.electacta.2015.08.016.
URL http://dx.doi.org/10.1016/j.electacta.2015.08.016

[80] M. M. Moghadam, J. M. Rickman, M. P. Harmer, H. M. Chan, The role of boundary variability in polycrystalline grain-boundary diffusion, Journal of Applied Physics 117 (4). doi:10.1063/1.4906778.
URL http://dx.doi.org/10.1063/1.4906778

[81] O. K. Johnson, C. A. Schuh, Texture mediated grain boundary network design in three dimensions, Mechanics of Materials 118 (September 2017) (2018) 94–105. doi:10.1016/j.mechmat.2017.12.001.
URL https://doi.org/10.1016/j.mechmat.2017.12.001

[82] M. Biscondi, Intergranular diffusion and grain-boundary structure, Physical Chemistry of the Solid State: Applications to Metals and their Compounds (1984) 225–239.

[83] J. Sommer, C. Herzig, S. Mayer, W. Gust, Grain Boundary Self-Diffusion in Silver Bicrystals (1989).

[84] K. V. Laven, Grid Sphere (2015).
URL https://www.mathworks.com/matlabcentral/fileexchange/28842-grid-sphere

[85] S. Weinzierl, Introduction to Monte Carlo methods (2000). arXiv:0006269.